

STOCHASTIC FUNCTIONAL ANALYSIS AND MULTILEVEL VECTOR FIELD ANOMALY DETECTION

JULIO E. CASTRILLÓN-CANDÁS[‡], MARK KON[‡]

ABSTRACT. Massive vector field datasets are common in multi-spectral optical and radar sensors, among many other emerging areas of application. In this paper we develop a novel *stochastic functional (data) analysis* approach for detecting anomalies based on the covariance structure of nominal stochastic behavior across a domain. An optimal vector field Karhunen-Loeve expansion is applied to such random field data. A series of multilevel orthogonal functional subspaces is constructed from the geometry of the domain, adapted from the KL expansion. Detection is achieved by examining the projection of the random field on the multilevel basis. In addition, reliable hypothesis tests are formed that do not require prior assumptions on probability distributions of the data. The method is applied to the important problem of deforestation and degradation in the Amazon forest. This is a complex non-monotonic process, as forests can degrade and recover. Using multi-spectral satellite data from Sentinel-2, the multilevel filter is constructed and anomalies are treated as deviations from the initial state of the forest. Forest anomalies are quantified with robust hypothesis tests. Our approach shows the advantage of using multiple bands of data in a vectorized complex, leading to better anomaly detection beyond the capabilities of scalar-based methods.

1. INTRODUCTION

The development of ever more massive datasets, concurrent with advances in artificial intelligence and machine learning, are transforming many aspects of society in extensive ways. Remote sensing and GIS data over various temporal and spatial resolutions provide foundational data for addressing issues within many of the facets of human dynamics [50]. Increasingly, Wi-Fi and GPS tracking via cell phones enable us to gather data at high spatio-temporal resolutions at low cost, providing real-time solutions for dynamic traffic management and accident prevention [42, 22]. Geotagged social media and direct locational information have provided ways of classifying functional characteristics of urban locations [12, 24]. Analysis of information from daily mobility patterns [5], IoT sensors [40], satellites [44] and drones [56], provide extensive data for systematic study of human dynamics in migration, disease outbreaks [41], and threat outbreaks. Many methods have been developed to detect and identify anomalies. In particular, for syndromic surveillance and signal processing the scan statistics approach has been widely used [2, 33, 13, 21, 36, 1, 20, 37]. In [31] the authors develop an approach to detect network anomalies based on residual spaces of a Principal Component Analysis. This approach is related to our method developed in this paper.

In this paper we develop a framework to detect anomalies in random vector fields based on stochastic functional analysis. This approach was recently introduced in [9] for scalar data and is here based on optimal vector field Karhunen-Loève (KL) tensor product expansions, and the construction of multilevel functional spaces for the detection of anomalies. In particular, it is well suited for vector field data over complex geometrical domains (or networks) arising from the measurement of different modalities from the same objects, including satellite data with multiple spectral bands. Using KL expansions, this approach allows detection within large classes of random vector fields. The nested multilevel spaces are natively adapted to tensor product expansions. Their

[‡] DEPARTMENT OF MATHEMATICS AND STATISTICS, BOSTON UNIVERSITY, BOSTON, MA
E-mail address: jcandas@bu.edu, mkon@bu.edu.

construction is elaborate and has been used elsewhere in the context of solving Partial Differential Equations. This approach has the following features:

- Detection of anomalous global and local signals described as scalar or vectorial random fields.
- Construction of reliable hypothesis tests with controllable distributions that do not require assumptions on the distribution of the data (important).
- Stochastic fusion of the anomalies in multimodal vector field data without any loss of information. This represents an optimal fusion of the scalar components of the vectorized data.
- Resulting native integration of multiple modalities with no loss of discriminatory power.
- Quantification of magnitudes of the anomalies defined on a suitable Bochner normed space.
- Adaptability of vector field signal domains to be defined on complex topologies. This includes geospatial, spatio-temporal, manifold and network topologies, among others.
- Multilevel filters can process large quantities of data with near-optimal performance.
- Augmentation of current statistical methods such as change point detection [4, 28, 38, 25, 35, 30, 14, 26, 19, 3, 53, 29, 39, 16, 49, 48, 57].
- Applicability of the theory and code to existing Machine Learning problems, leading to significant increases to accuracy in their solutions. [10].
- A fully non-parametric probabilistic framework, in particular without any Gaussian assumptions.

We introduce a novel application of this framework in the context of a major environmental problem, deforestation in the Amazon rain forest. Proper detection of deforestation and forest degradation events can lead to quantification and potential mitigation of resulting effects on climate. Climate change is understood to be driven by unmitigated anthropogenic emissions of greenhouse gases into the atmosphere, primarily of carbon dioxide from combustion of fossil fuels and deforestation. Effects of climate change are being witnessed now, are believed to be irreversible on the timescale of human lifespan, and are projected to increase in the decades to come [55]. Additionally, deforestation has been identified as a factor of greater significance than climate change alone [51], and in fact as the single most important variable affecting ecological systems [11] and the most significant threat to biodiversity [46].

Satellite remote sensing is often the only viable means for gathering deforestation information, but numerous problems hinder effective collection of information. Among the technical problems are persistent and unpredictable cloud cover in deforestation hot-spots, which complicates automated processing of very accessible optical satellite data.

Our mathematical framework is well suited to detecting changes on land surfaces in optical modalities. An application of the multilevel anomaly filter to such data (e.g., collected by the Sentinel-2 satellite) recording Amazon forest degradation is illustrated in Figures 4 and 9. This example illustrates the complexity of detecting such degradation: the logging of the forest in Figure 4 on day 3484 does not change the actual level of land cover remaining as forest. Further, the forest does not stay in a degraded state, but is then allowed to recover. Note that both the initial degradation event (driven by selective logging) and the subsequent recovery can be detected by the filter. Also note that the anomaly introduced by imperfect cloud masking at day 3909 is easy to detect as fictitious due to its contrast with temporal behavior of forest degradation. In this example the filter operates on a time series of 71 Sentinel-2 images in an area covered by 150×150 ten meter pixels. More specifically, starting from day 1 to day 3200, the covariance structure and multilevel anomaly filter were built from measurements based on the Enhanced Vegetation Index (EVI), from satellite data. The multilevel filter is then applied to each of the 71 Sentinel-2 images starting from day 3300, and an anomaly map is constructed from our KL approach. Figure 9 illustrates the tracking of the forest degradation anomaly, in this case at pixel (66,108). Our work

here augments this approach to vector field data, i.e. structured multiple features. The detection framework thus extends multiple satellite detection modalities (e.g., multi-spectral data) allowing augmented coordinated detection over scalar modalities, e.g., in EVI data (See Figure 11). The deforestation and degradation detection problem can thus be framed in a precisely stated and much more general mathematical framework, using high dimensional probabilistic constructions.

2. VECTOR FIELD KARHUNEN LOÈVE

The Karhunen-Loève expansion is an important methodology that represents random fields in terms of spatial-stochastic tensor expansions. It has been shown to be optimal in several ways, making it attractive for analysis of random fields. We are interested in data that can be modeled as random vector fields, for example satellite sensors with multiple spectral bands forming naturally vectorized data, among many such examples. In this section the mathematical background for the vector field KL expansion is introduced.

Let U be a domain of \mathbb{R}^d , $d \in \mathbb{N}$, and $(\Omega, \mathcal{F}, \mathbb{P})$ be a complete probability space, with a set of outcomes Ω , and \mathcal{F} a σ -algebra of events equipped with the probability measure \mathbb{P} . Let $L^2(U; \mathbb{R}^q)$ be the space of all square integrable functions $\mathbf{v} : U \rightarrow \mathbb{R}^q$ equipped with the standard inner product $(\mathbf{u}, \mathbf{v}) = \int_U \mathbf{u}^T \mathbf{v} \, d\mathbf{x}$, for all $\mathbf{u}, \mathbf{v} \in L^2(U; \mathbb{R}^q)$, where $\mathbf{v}(\mathbf{x}) = [v_1(\mathbf{x}), \dots, v_q(\mathbf{x})]^T$ and $v_i \in L^2(U) := L^2(U; \mathbb{R})$ for $i = 1, \dots, q$.

Taking uncertainty into account, suppose that the data can be described as random vector field $\mathbf{v} : \Omega \rightarrow L^2(U; \mathbb{R}^q)$, where $\mathbf{v}(\mathbf{x}, \omega) = [v_1(\mathbf{x}, \omega), \dots, v_d(\mathbf{x}, \omega)]^T$, $\mathbf{x} \in U$, $\omega \in \Omega$, and $v_i(\mathbf{x}, \cdot) \in L^2(\Omega)$ for $i = 1, \dots, q$. Note that from context it will be clear when $\mathbf{v}(\mathbf{x})$ and $\mathbf{v}(\mathbf{x}, \omega)$ is referenced. Let $L^2_{\mathbb{P}}(\Omega; L^2(U; \mathbb{R}^q))$ be the space of all strongly measurable functions $\mathbf{v} : \Omega \rightarrow L^2(U; \mathbb{R}^q)$ equipped with the inner product $(\mathbf{u}, \mathbf{v})_{L^2_{\mathbb{P}}(\Omega; L^2(U))} = \int_{\Omega} (\mathbf{u}, \mathbf{v}) \, d\mathbb{P}$, for all $\mathbf{u}, \mathbf{v} \in L^2_{\mathbb{P}}(\Omega; L^2(U; \mathbb{R}^d))$.

Definition 2.1.

- (a) Suppose $\mathbf{v} \in L^2_{\mathbb{P}}(\Omega; L^2(U; \mathbb{R}^q))$, and denote $\mathbb{E}[\mathbf{v}] := [\mathbb{E}[v_1], \dots, \mathbb{E}[v_q]]$ as the mean of $\mathbf{v}(\mathbf{x}, \omega)$, where $\mathbb{E}[v_i] := \int_{\Omega} v_i(\mathbf{x}, \omega) \, d\mathbb{P}$, for $i = 1, \dots, q$.
- (b) For all $\mathbf{v} \in L^2_{\mathbb{P}}(\Omega; L^2(U; \mathbb{R}^q))$ let $\text{Cov}(v_i(\mathbf{x}, \omega), v_j(\mathbf{y}, \omega)) := \mathbb{E}[(v_i(\mathbf{x}, \omega) - \mathbb{E}[v_i(\mathbf{x}, \omega)]) (v_j(\mathbf{y}, \omega) - \mathbb{E}[v_j(\mathbf{y}, \omega)])]$ for $i, j = 1, \dots, q$, and denote the matrix-valued covariance function of \mathbf{v} as $\text{Cov}(\mathbf{v}(\mathbf{x}), \mathbf{v}(\mathbf{y})) :=$

$$\begin{bmatrix} \text{Cov}(v_1(\mathbf{x}, \omega), v_1(\mathbf{y}, \omega)) & \text{Cov}(v_1(\mathbf{x}, \omega), v_2(\mathbf{y}, \omega)) & \dots & \text{Cov}(v_1(\mathbf{x}, \omega), v_q(\mathbf{y}, \omega)) \\ \text{Cov}(v_2(\mathbf{x}, \omega), v_1(\mathbf{y}, \omega)) & \text{Cov}(v_2(\mathbf{x}, \omega), v_2(\mathbf{y}, \omega)) & \dots & \text{Cov}(v_2(\mathbf{x}, \omega), v_q(\mathbf{y}, \omega)) \\ \vdots & \vdots & \ddots & \vdots \\ \text{Cov}(v_q(\mathbf{x}, \omega), v_1(\mathbf{y}, \omega)) & \text{Cov}(v_q(\mathbf{x}, \omega), v_2(\mathbf{y}, \omega)) & \dots & \text{Cov}(v_q(\mathbf{x}, \omega), v_q(\mathbf{y}, \omega)) \end{bmatrix}.$$

From the properties of Bochner integrals (see [32, 23]) we have that $\mathbb{E}[v(\mathbf{x}, \omega)] \in L^2(U; \mathbb{R}^q)$ and that the covariance function $\text{Cov}(v_i(\mathbf{x}, \omega), v_j(\mathbf{y}, \omega)) \in L^2(U \times U)$ for all $i, j = 1, \dots, q$. Thus $\text{Cov}(\mathbf{v}(\mathbf{x}, \omega), \mathbf{v}(\mathbf{y}, \omega)) \in L^2(U \times U; \mathbb{R}^{q \times q})$, where the space $L^2(U \times U; \mathbb{R}^{q \times q})$ is equipped with the inner product

$$(\mathbf{A}, \mathbf{B})_{L^2(U \times U; \mathbb{R}^{q \times q})} := \int_U \int_U \mathbf{1}^T \mathbf{A}(\mathbf{x}, \mathbf{y}) \bullet \mathbf{B}(\mathbf{x}, \mathbf{y}) \, d\mathbf{x} d\mathbf{y}$$

for all $\mathbf{A}, \mathbf{B} \in L^2(U \times U; \mathbb{R}^{q \times q})$, where $\mathbf{1}$ is a q dimensional vector with all entries equal to one and $\mathbf{A} \bullet \mathbf{B}$ corresponds to the Hadamard product of \mathbf{A} and \mathbf{B} .

Although Karhunen-Loève expansions are well understood for the scalar case, rigorous proofs and studies of optimality properties for the vector field case have been somewhat sparse. Despite the popularity of the KL expansion and its multiple references, a rigorous existence and optimality proof for the vector field case could not be found except for the detailed analysis in [47], in the context of tensor products. Suppose that H, S are separable Hilbert spaces with the inner products $(\cdot, \cdot)_H$ and $(\cdot, \cdot)_S$ respectively. Any element $f \in H \otimes S$ can be written as a convergent series of the form $f = \sum_{k \in \mathbb{N}} f_k \otimes s_k$ with the associated correlation $C_f := \sum_{k \in \mathbb{N}} f_k \otimes f_k$. From Theorem 2.3 in

[47] there is a one-to-one correspondence between C_f and positive definite trace class operators in C_f in H . From the spectral expansion of C_f , Theorems 2.5 and 2.7 then show the existence of the KL expansion and the corresponding optimality properties.

Remark. To apply these theorems we set $H := L^2(U; \mathbb{R}^q)$ and $S := L^2_{\mathbb{P}}(\Omega)$. However, we need to clearly show what is meant by the tensor product spaces $L^2(U; \mathbb{R}^q) \otimes L^2_{\mathbb{P}}(\Omega)$ and $L^2(U; \mathbb{R}^q) \otimes L^2(U; \mathbb{R}^q)$. The proofs for Propositions 2.2, 2.3 and 2.4 are based on the arguments given in Chapter II.4 from [43] and extended to the vector field case. The proofs are contained in the [Appendix](#).

Proposition 2.2. *Let $\{\mathbf{v}_k\}_{k \in \mathbb{N}}$ be a complete orthonormal basis of $L^2(U; \mathbb{R}^q)$. Then $\{\mathbf{v}_k(\mathbf{x})\mathbf{v}_l(\mathbf{y})^T\}_{k,l \in \mathbb{N}}$ is a complete orthonormal basis for $L^2(U \times U; \mathbb{R}^{q \times q})$.*

Proposition 2.3. *$L^2(U; \mathbb{R}^q) \otimes L^2(U; \mathbb{R}^q)$ is isomorphic to $L^2(U \times U; \mathbb{R}^{q \times q})$.*

Proposition 2.4. *$L^2(U; \mathbb{R}^q) \otimes L^2_{\mathbb{P}}(\Omega)$ is isomorphic to $L^2_{\mathbb{P}}(\Omega; L^2(U; \mathbb{R}^q))$.*

Consider the operator

$$\mathcal{C}_{\mathbf{v}}(\mathbf{u})(\mathbf{x}) := \int_U \text{Cov}(v(\mathbf{x}, \omega), v(\mathbf{y}, \omega)) \mathbf{u}(\mathbf{y}) \, d\mathbf{y}$$

for all $\mathbf{u} \in L^2(U; \mathbb{R}^q)$. From Lemma 2 in [23] operator $\mathcal{C}_{\mathbf{v}} : L^2(U; \mathbb{R}^q) \rightarrow L^2(U; \mathbb{R}^q)$ is a non-negative symmetric, trace class operator. From Theorem 1 in [23] there exists an orthonormal set of eigenfunctions $\{\phi_k\}_{k \in \mathbb{N}}$, where $\phi_k \in L^2(U; \mathbb{R}^q)$, and eigenvalues $\lambda_1 \geq \lambda_2 \geq \dots \geq 0$ such that $\mathcal{C}_{\mathbf{v}}\phi_k = \lambda_k\phi_k$ for all $k \in \mathbb{N}$. Furthermore, for any $\mathbf{u} \in L^2(U; \mathbb{R}^q)$ we have that $\mathcal{C}_{\mathbf{v}}(\mathbf{u}) = \sum_{k \in \mathbb{N}} \lambda_k(\mathbf{u}, \phi_k)_{L^2(U; \mathbb{R}^q)} \phi_k$.

Since $\mathcal{C}_{\mathbf{v}}$ is a trace class operator (e.g. $\sum_{k \in \mathbb{N}} \lambda_k < \infty$), from the argument given in Theorem 2.3 in [47] the series $\sum_{k \in \mathbb{N}} \lambda_k^{\frac{1}{2}} \phi_k \otimes s_k$ converges to an element $f \in L^2(U; \mathbb{R}^q) \otimes L^2(\Omega)$, where $\{s_k\}_{k \in \mathbb{N}}$ is a complete orthonormal basis for $L^2_{\mathbb{P}}(\Omega)$, and $C_f = \sum_{k \in \mathbb{N}} \lambda_k \phi_k \otimes \phi_k$. Now let

$$C_{\mathbf{v}} := \sum_{k \in \mathbb{N}} \lambda_k \phi_k \phi_k^T.$$

From Proposition 2.3 and the identity $(\mathcal{C}_{\mathbf{v}}\mathbf{u}, \mathbf{w})_H = (C_f, \mathbf{u} \otimes \mathbf{w})_{H \otimes H}$, for all $\mathbf{u}, \mathbf{w} \in H := L^2(U; \mathbb{R}^q)$ we have $(\mathcal{C}_{\mathbf{v}}\mathbf{u}, \mathbf{w})_H = (C_{\mathbf{v}}, \mathbf{u}\mathbf{w}^T)_{L^2(U \times U; \mathbb{R}^{q \times q})}$. Since $\{\mathbf{v}_k\mathbf{v}_l^T\}_{k,l \in \mathbb{N}}$ is a complete orthonormal basis for $L^2(U \times U; \mathbb{R}^{q \times q})$ we conclude that $\text{Cov}(\cdot, \cdot) = C_{\mathbf{v}}$ almost everywhere. From Proposition 2.4 and Theorem 2.5 [47] the KL expansion for the vector field data is obtained:

Theorem 2.5. *Suppose $\mathbf{v} \in L^2_{\mathbb{P}}(\Omega; L^2(U; \mathbb{R}^q))$ then*

$$\mathbf{v}(\mathbf{x}, \omega) = \mathbb{E}[\mathbf{v}(\mathbf{x}, \omega)] + \sum_{k \in \mathbb{N}} \lambda_k^{\frac{1}{2}} \phi_k(\mathbf{x}) Y_k(\omega),$$

where $Y_k(\omega) = \frac{1}{\sqrt{\lambda_k}} \int_U (\mathbf{v}(\mathbf{x}, \omega) - \mathbb{E}[\mathbf{v}(\mathbf{x}, \omega)])^T \phi_k(\mathbf{x}) \, d\mathbf{x}$, $\mathbb{E}[Y_k Y_l] = \delta_{kl}$ and $\mathbb{E}[Y_k] = 0$ for all $k, l \in \mathbb{N}$.

The KL expansion has the useful property of being optimal in the set of all product expansions. Suppose that $H_M \subset L^2(U)$ is a finite dimensional subspace of $L^2(U)$ such that $\dim H_M = M$ and $P_{H_M \otimes L^2_{\mathbb{P}}(\Omega)} : L^2(U; \mathbb{R}^q) \otimes L^2_{\mathbb{P}}(\Omega) \rightarrow H_M \otimes L^2_{\mathbb{P}}(\Omega)$ is an orthogonal projection operator. Suppose $\mathbf{v} \in L^2(U; \mathbb{R}^q) \otimes L^2_{\mathbb{P}}(\Omega)$, with $\mathbb{E}[\mathbf{v}] = 0$, then from Theorem 2.7 in [47]

$$\inf_{\substack{H_M \subset L^2(U; \mathbb{R}^q) \\ \dim H_M = M}} \|\mathbf{v} - P_{H_M \otimes L^2_{\mathbb{P}}(\Omega)} \mathbf{v}\|_{L^2_{\mathbb{P}}(\Omega) \otimes L^2(U)} = \left(\sum_{k \geq M+1} \lambda_k \right)^{\frac{1}{2}}$$

where the infimum is achieved only when $H_M = \text{span}\{\phi_1, \dots, \phi_M\}$.

Remark. In practice the KL expansion of a random field is intractable for even a modest number of terms. Estimating the joint distribution of Y_1, \dots, Y_M requires massive amounts of data due to the high dimensionality. Only under certain conditions, such as for Gaussian processes, can the random variables Y_1, \dots, Y_M be explicitly known (and shown to be independent). However, for the

anomaly filter built in this paper, the joint distribution of Y_1, \dots, Y_M is not required. Furthermore, for the hypothesis test derived in section 3 only the eigenpairs (λ_k, ϕ_k) for $k = 1, \dots, M$ are needed. This makes for a significantly easier problem whose quantities can be estimated in practice from realizations of the random field $\mathbf{v}(\mathbf{x}, \omega) \in L^2_{\mathbb{P}}(\Omega; L^2(U; \mathbb{R}^q))$ using the method of snapshots [6].

3. ANOMALY DETECTION AND MULTILEVEL ORTHOGONAL EIGENSPPACES

The KL expansion provides a mechanism to represent a vector valued random field $\mathbf{v}(\mathbf{x}, \omega)$ in terms of optimal approximations based on the first M terms: $\mathbf{v}_M(\mathbf{x}, \omega) - \mathbb{E}[\mathbf{v}] = \sum_{k=1}^M \lambda_k^{\frac{1}{2}} \phi_k(\mathbf{x}) Y_k(\omega)$. In the rest of the discussion, without loss of generality, it is assumed that $\mathbb{E}[\mathbf{v}] = \mathbf{0}$. Suppose that $\mathbf{u}(\mathbf{x}, \omega)$ is an observable random field and assume that the model is given by $\mathbf{u}(\mathbf{x}, \omega) = \mathbf{v}_M(\mathbf{x}, \omega) + \mathbf{w}(\mathbf{x}, \omega)$. Given knowledge of the eigenstructure of $\mathbf{v}_M(\mathbf{x}, \omega)$ and the observations $\mathbf{u}(\mathbf{x}, \omega)$, the goal is detection of the anomalous process $\mathbf{w}(\mathbf{x}, \omega)$ and its quantification with respect to a suitable norm. Detection is achieved by the construction of multilevel spaces that are adapted to local and global components of $\{\phi_1, \dots, \phi_M\}$.

Assumption 3.1. We let $\mathbf{V}_0 := \text{span}\{\phi_1, \phi_2, \dots, \phi_M\}$ and $\mathbf{V}_0 \subset \mathbf{V}_1 \subset \dots \subset L^2(U; \mathbb{R}^q)$ be a sequence of nested subspaces in $L^2(U; \mathbb{R}^q)$ such that $\bigcup_{k \in \mathbb{N}_0} \mathbf{V}_k = L^2(U; \mathbb{R}^q)$. Furthermore, for all $k \in \mathbb{N}$, we let $\mathbf{W}_k \subset L^2(U; \mathbb{R}^q)$ be a subspace such that $\mathbf{V}_{k+1} = \mathbf{V}_k \oplus \mathbf{W}_k$, where \oplus is the direct sum, so that $\mathbf{V}_0 \oplus \bigoplus_{k \in \mathbb{N}_0} \mathbf{W}_k = L^2(U; \mathbb{R}^q)$.

Although the definition of these spaces is relatively simple, the construction is elaborate with heavy notation and based on differential operator-adapted multilevel methods from scientific computing and computational applied mathematics, for solution of Partial Differential Equations [17, 7]. The details of construction of these multilevel spaces for random fields on complex geometries can be found our recent publication [9] for the scalar case. Here we extend this optimal decomposition to multidimensional vector fields.

We will assume that U can be decomposed into simplices, which can be thought as generalizations of triangulations to arbitrary dimensions. This allows complex geometric shapes to be simply approximated. First we give some definitions.

Definition 3.2. A k -simplex is defined to be a convex hull of vertices $z_0, z_1, \dots, z_k \in \mathbb{R}^k$ that are affinely independent.

Definition 3.3.

- i) We denote \mathbf{x}_i to be the barycenters of simplices $\tau_i \in \mathcal{T}$ and define $\mathbb{S} := \{\mathbf{x}_1, \dots, \mathbf{x}_N\}$.
- ii) The face of a k -simplex is the convex hull of any $m + 1$ subset of the points that define a k -simplex.

Definition 3.4. Suppose that \mathcal{T} is a collection of simplices in \mathbb{R}^d . Then \mathcal{T} is a k -simplicial complex if the following properties are satisfied:

- i) Every face of a simplex in \mathcal{T} is also in \mathcal{T} .
- ii) The non-empty intersection of any two simplices $\tau_1, \tau_2 \in \mathcal{T}$ is a face of both τ_1 and τ_2 .
- iii) The highest dimension of any simplex in \mathcal{T} is $k \leq d$.

The following assumption allows us to construct complex geometrical shapes from the k -simplices and define a space of functions \mathbf{V}_{n+1} on them that approximates the vector field $v(\mathbf{x}, \omega)$. In Figure 1 an example of triangulation of a surface constructed from 2-simplices (triangles) is shown.

Assumption 3.5.

- i) $U = \bigcup_{\tau_i \in \mathcal{S}} \tau_i$, where \mathcal{S} is a subset of \mathcal{T} and contains N simplices of order k .
- ii) For any simplex $\tau_i \in \mathcal{S}$ and $j = 1, \dots, q$ let $\chi_i^j := c_i^j[0, \dots, 0, 1_{\tau_i}^j, 0, \dots, 0]$, where $\chi_i^j \in L^2(U; \mathbb{R}^q)$ and $1_{\tau_i}^j$ corresponds to the indicator function at the j^{th} entry in the vector χ_i^j on the simplex τ_i .
- iii) The coefficients c_i^j for $i = 1, \dots, N$ and $j = 1, \dots, q$ are chosen such that collection of functions χ_i^j , $\mathcal{E} := \{\{\chi_i^j\}_{i=1}^N\}_{j=1}^q$, forms an orthonormal set in $L^2(U; \mathbb{R}^q)$.

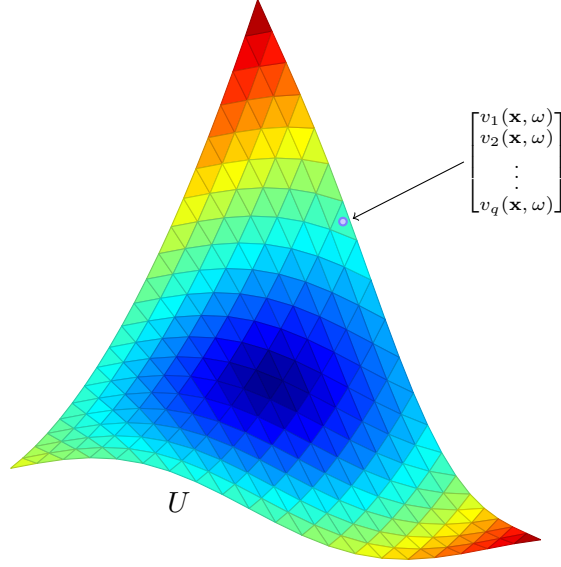


FIGURE 1. Surface domain U constructed from 2-simplicies (triangles) in \mathbb{R}^3 . The vector random field $\mathbf{v}(\mathbf{x}, \omega) \in L^2_{\mathbb{P}}(\Omega; L^2(U; \mathbb{R}^q))$ is defined over the domain U . As an example this could be satellite multi-spectral data over land.

- iv) Let $\mathbf{V}_{n+1} = \mathcal{P}(\mathcal{E}) := \text{span}\{\chi_i^l\}$. We assume that Karhunen-Loève eigenfunctions $\phi_i \in \mathcal{P}(\mathcal{E})$ for all $i = 1, \dots, M$ where $N > M$.

From the set of indicator functions in \mathcal{E} , a multilevel basis representation can be constructed that is adapted to the geometry of the domain U and the eigenfunctions $\{\phi_1, \phi_2, \dots, \phi_M\}$. This will allow detection of signals in the vector field in a local and global sense. The algorithm to construct a multilevel basis for the scalar case is described in detail in [9]. The extension of this basis to the vector field case can be essentially obtained by replacing the $L^2(U)$ inner product with that in $L^2(U; \mathbb{R}^q)$.

For the sake of completeness the algorithm building the binary tree is described here in detail. We will then show how the multilevel basis is constructed for vector field data. A binary tree is constructed to locate efficiently the simplicies in \mathcal{S} at different levels of resolution. Furthermore the binary tree will serve as a base to construct and locate the multilevel basis functions of the spaces \mathbf{W}_k for $k = 0, \dots, n-1$. The domain U is initially assumed to be embedded in a square cell of unit length. For N this can be easily done with a rescaling. We follow that procedure described in [15] for the construction of a kd-tree type decomposition. Other options include Random Projection (RP) trees, which can be found in [15].

Suppose that all the barycenters $\mathbf{x} \in \mathbb{S}$ are embedded in the cell the root cell B_{root}^0 (or B_0^0) $\subset \mathbb{R}^d$, which corresponds to the top of the binary tree. Without loss of generality it can be assumed that $B_{\text{root}}^0 = [0, 1]^d$ and $\mathbb{S} \subset B_{\text{root}}^0$. Now, the root cell is subdivided according to the rule in Algorithm 2 in Figure 2, thus forming two new cells B_{left}^1 and B_{right}^1 at level 1. In general for any cell B_k^l at level l and index k the collection of barycenters $\tilde{\mathbb{S}} = \{\mathbf{x}_j | \mathbf{x}_j \in B_k^l\}$ is subdivided as follows by using the following rule [15] (Algorithm 2 in Figure 2):

- Suppose v_i is the unit vector in the axis coordinate direction for $i = 1, \dots, q$.
- For each coordinate direction $i = 1, \dots, q$ project every barycenter $\mathbf{x}_i \in \tilde{\mathbb{S}}$ onto the unit vector v_i

Algorithm 1 MakeTree(\mathbb{S}) function

```

1: procedure MAKETREE( $\mathbb{S}, n_0$ )
2:   if root then
3:      $k \leftarrow 0, l \leftarrow 0, \tilde{\mathbb{S}} \leftarrow \{\mathbf{x}_j | \mathbf{x}_j \in \mathbb{S}\}$ 
4:      $T \leftarrow \text{MakeTree}(\tilde{\mathbb{S}}, n_0, k, l)$ 
5:   else
6:      $T.B_k^l \leftarrow \{\mathbf{x} | \mathbf{x} \in \tilde{\mathbb{S}}\}$ 
7:      $T.k \leftarrow k$ 
8:      $T.l \leftarrow l, k \leftarrow k + 1, l \leftarrow l + 1$ 
9:     if  $|\tilde{\mathbb{S}}| < n_0$  then return (Leaf)
10:     $(\text{Rule}, \text{threshold}, v) \leftarrow \text{CR}(\tilde{\mathbb{S}})$ 
11:     $(T.\text{LeftTree}, k) \leftarrow \text{MakeTree}$ 
12:     $(\mathbf{x} \in \tilde{\mathbb{S}}: \text{Rule}(\mathbf{x}) = \text{True}, n_0, k, l + 1)$ 
13:     $(T.\text{RightTree}, k) \leftarrow \text{MakeTree}$ 
14:     $(\mathbf{x} \in \tilde{\mathbb{S}}: \text{Rule}(\mathbf{x}) = \text{false}, n_0, k, l + 1)$ 
15:     $T.\text{threshold} \leftarrow \text{threshold}, T.v \leftarrow v$ 

```

Algorithm 2 ChooseRule($\tilde{\mathbb{S}}$) function for kD-tree where $\tilde{\mathbb{S}} \subset \mathbb{S}$.

```

1: procedure CHOOSERULE( $\tilde{\mathbb{S}}$ )
2:   Choose a coordinate direction
   that has maximal variance of the
   projection of the points in  $\tilde{\mathbb{S}}$ .
3:   Rule( $\mathbf{x}$ ) :=  $\mathbf{x} \cdot v \leq \text{threshold} =$ 
   median

```

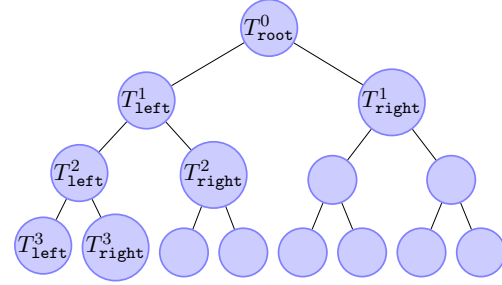


FIGURE 2. Binary tree construction algorithm from the simplicies in \mathcal{S} used to construct the domain U . Algorithm 2 is used to decide how the barycenters in $\tilde{\mathbb{S}}$ (B_l^k) are split. The tree structure T is built from Algorithm 1 and 2 and is constructed recursively until there are at most $n_0 - 1$ barycenters left in the cell B_k^l . Once all the leaves are reached the algorithm stops. Notice that the list of barycenters $\tilde{\mathbb{S}}$ at any level $l > 0$ is updated with the barycenters that satisfy $\text{Rule}(\mathbf{x})$ or do not satisfy $\text{Rule}(\mathbf{x})$.

- (c) Compute the sample variance of these projection coefficients for each coordinate unit vector v_i .
- (d) Choose the unit coordinate vector v_i in the direction $1 \leq j \leq d$ with the maximal sample variance for the above projection coefficients.
- (e) Compute the median of the projections along v and split the cell in two parts (B_{left}^{l-1} and B_{right}^{l-1}) at this coordinate position.

By applying Algorithm 1 we obtain a tree structure T , which contains all the cells B_k^l at each level of resolution $l = 0, \dots, n$ for every level l and associated index k . Furthermore, let \mathcal{B} be the collection of all the non-empty cells B in the tree T and $\mathcal{B}^l := \{B_m^j \in \mathcal{B} | j = l\}$. From the tree structure T and the set \mathcal{E} the multilevel basis adapted to the vector field KL expansion can be constructed.

We first show how to construct the multilevel basis functions at the finest level n (or leaf). Suppose that $B_k^n \in \mathcal{B}^n$, and after reordering of the numbering of the barycenters suppose that $\{\mathbf{x}_1, \dots, \mathbf{x}_s\}$ are the barycenters contained in B_k^n . For each simplex τ_i with corresponding barycenter \mathbf{x}_i there exist $\chi_i^1, \dots, \chi_i^q$ as orthonormal functions. Thus we form the orthonormal set $\mathcal{E}_n^q := \{\chi_1^1, \chi_2^1, \dots, \chi_q^1, \chi_1^2, \chi_2^2, \dots, \chi_q^2, \dots, \chi_1^{s_{n,k}}, \chi_2^{s_{n,k}}, \dots, \chi_q^{s_{n,k}}\}$. The objective is to form a linear combination of the elements in \mathcal{E}_n^q ; we will construct a multilevel grid with the desired properties. To

this end let

$$\begin{aligned}\phi_j^{n,k} &:= \sum_{i=1}^{s_{n,k}} \sum_{h=1}^q c_{i,h,j}^{n,k} \chi_i^h, \quad j \in \{1, \dots, a_{n,k}\} \\ \psi_j^{n,k} &:= \sum_{i=1}^{s_{n,k}} \sum_{h=1}^q d_{i,h,j}^{n,k} \chi_i^h, \quad j \in \{a_{n,k} + 1, \dots, s_{n,k}q\},\end{aligned}$$

where the coefficients $c_{i,h,j}^{n,k}, d_{i,h,j}^{n,k}, a_{n,k} \in \mathbb{R}$ are still unknown. The goal is to construct $\psi_j^{n-1,k}$ such that it is orthogonal to the subspace \mathbf{V}_0 under the $L^2(U; \mathbb{R}^q)$ inner product, i.e. for $i = 1, \dots, M$ and $j = a_{n,k} + 1, \dots, s_{n,k}q$,

$$(1) \quad \int_U \phi_i(\mathbf{x})^\top \psi_j^{n,k}(\mathbf{x}) d\mathbf{x} = 0.$$

From the eigenfunctions ϕ_1, \dots, ϕ_M of the KL expansion and \mathcal{E}_k^n we can form the matrix

$$\mathbf{M}^{n,k} := \begin{bmatrix} (\phi_1(\mathbf{x}), \chi_1^1(\mathbf{x})) & \dots & (\phi_1(\mathbf{x}), \chi_1^{s_{n,k}}(\mathbf{x})) & \dots & (\phi_1(\mathbf{x}), \chi_q^1(\mathbf{x})) & \dots & (\phi_1(\mathbf{x}), \chi_q^{s_{n,k}}(\mathbf{x})) \\ (\phi_2(\mathbf{x}), \chi_1^1(\mathbf{x})) & \dots & (\phi_2(\mathbf{x}), \chi_1^{s_{n,k}}(\mathbf{x})) & \dots & (\phi_2(\mathbf{x}), \chi_q^1(\mathbf{x})) & \dots & (\phi_2(\mathbf{x}), \chi_q^{s_{n,k}}(\mathbf{x})) \\ \vdots & \vdots & \vdots & \vdots & \vdots & \vdots & \vdots \\ (\phi_M(\mathbf{x}), \chi_1^1(\mathbf{x})) & \dots & (\phi_M(\mathbf{x}), \chi_1^{s_{n,k}}(\mathbf{x})) & \dots & (\phi_M(\mathbf{x}), \chi_q^1(\mathbf{x})) & \dots & (\phi_M(\mathbf{x}), \chi_q^{s_{n,k}}(\mathbf{x})) \end{bmatrix},$$

where (\cdot, \cdot) is the standard $L^2(U; \mathbb{R}^q)$ inner product. From the matrix $\mathbf{M}^{n,k}$ the coefficients $c_{i,h,j}^{n,k}, d_{i,h,j}^{n,k}, a_{n,k} \in \mathbb{R}$ can be computed. To this end apply the Singular Value Decomposition (SVD) to $\mathbf{M}^{n,k}$

$$(2) \quad \mathbf{M}^{n,k} = \mathbf{U} \mathbf{D} \mathbf{V}^\top,$$

where $\mathbf{U} \in \mathbb{R}^{M \times M}$, $\mathbf{D} \in \mathbb{R}^{M \times s_{n,k}}$, $\mathbf{V} \in \mathbb{R}^{s_{n,k} \times s_{n,k}}$, and let $a_{n,k}$ be the rank of the matrix $\mathbf{M}^{n,k}$, i.e. the number of non-zero singular values of the matrix \mathbf{D} . Our choices of coefficients $c_{i,h,j}^{n,k}$ and $d_{i,h,j}^{n,k}$

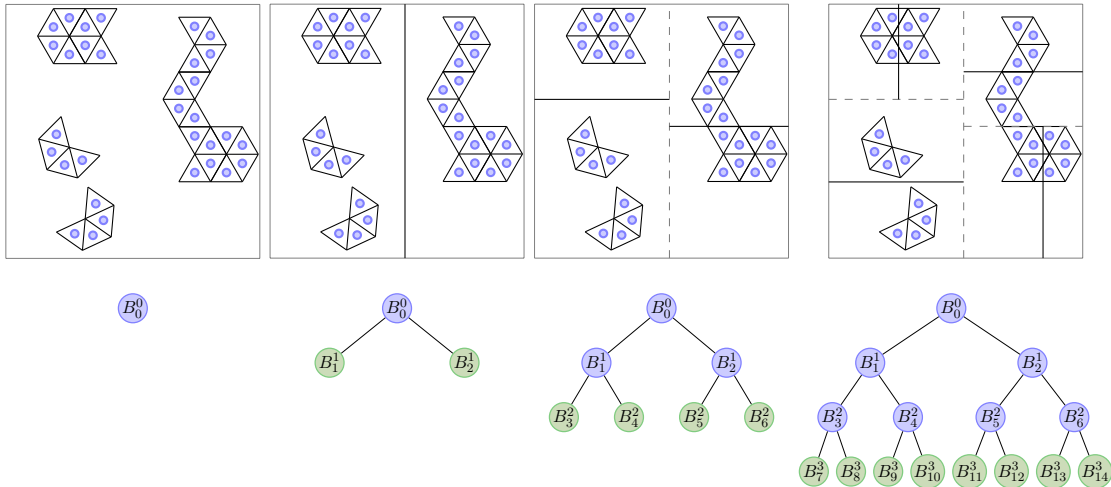


FIGURE 3. Cartoon example of the construction of a kd-tree from the triangular simplices in \mathcal{T} .

are now set to:

$$(3) \quad \left[\begin{array}{ccc|ccc} c_{1,1,1}^{n,k} & \cdots & c_{1,q,a_{n,k}}^{n,k} & d_{1,1,a_{n,k}+1}^{n,k} & \cdots & d_{1,1,s_{n,k}q}^{n,k} \\ c_{2,1,1}^{n,k} & \cdots & c_{2,1,a_{n,k}}^{n,k} & d_{2,1,a_{n,k}+1}^{n,k} & \cdots & d_{2,1,s_{n,k}q}^{n,k} \\ \vdots & \vdots & \vdots & \vdots & \vdots & \vdots \\ c_{s,q,1}^{n,k} & \cdots & c_{s,q,a_{n,k}}^{n,k} & d_{s,q,a_{n,k}+1}^{n,k} & \cdots & d_{s,q,s_{n,k}q}^{n,k} \end{array} \right] := \mathbf{V}.$$

Lemma 3.6. *Under this choice (equation (3)), $\psi_{a_{n,k}+1}^{n,k}, \dots, \psi_{s_{n,k}q}^{n,k}$ satisfy equation (1).*

Proof. Following the argument in [52, 8], let

$$\mathbf{N}^{n,k} := \left[\begin{array}{ccc|ccc} (\phi_1, \phi_1^{n,k}) & \cdots & (\phi_1, \phi_{a_{n,k}}^{n,k}) & (\phi_1, \psi_{a_{n,k}+1}^{n,k}) & \cdots & (\phi_1, \psi_{s_{n,k}q}^{n,k}) \\ \vdots & \ddots & \vdots & \vdots & \ddots & \vdots \\ (\phi_M, \phi_1^{n,k}) & \cdots & (\phi_M, \phi_{a_{n,k}}^{n,k}) & (\phi_M, \psi_{a_{n,k}+1}^{n,k}) & \cdots & (\phi_M, \psi_{s_{n,k}q}^{n,k}) \end{array} \right].$$

Thus from the choice of coefficients $c_{i,h,j}^{n,k}$ and $d_{i,h,j}^{n,k}$ we have that $\mathbf{N}^{n,k} = \mathbf{M}^{n,k} \mathbf{V}$. From equation (2) we conclude that $\mathbf{N}^{n,k} = \mathbf{M}^{n,k} \mathbf{V} = \mathbf{U} \mathbf{D}$. Since $\mathbf{M}^{n,k}$ is of rank $a_{n,k}$ we have $\mathbf{D} = [\mathbf{\Sigma} | \mathbf{0}]$, where $\mathbf{\Sigma} \in \mathbb{R}^{M \times a_{n,k}}$ is a diagonal matrix with the non-zero singular values of $\mathbf{M}^{n,k}$ and $\mathbf{0} \in \mathbb{R}^{M \times (s_{n,k}q - a_{n,k})}$ is the zero matrix. Thus $\mathbf{U} \mathbf{D} = [\mathbf{U} \mathbf{\Sigma} | \mathbf{0}]$ and $\mathbf{N}^{n,k} = [\mathbf{U} \mathbf{\Sigma} | \mathbf{0}]$. It follows that columns $a_{n,k}+1, \dots, s_{n,k}q$ of \mathbf{V} form an orthonormal basis of the nullspace of $\mathbf{M}^{n,k}$ and therefore $\psi_{a_{n,k}+1}^{n,k}, \dots, \psi_{s_{n,k}q}^{n,k}$ satisfy equation (1). \square

Lemma 3.7. *Let $D_k^n := \{\psi_{a_{n,k}+1}^{n,k}, \dots, \psi_{s_{n,k}q}^{n,k}\}$ and $C_k^n := \{\phi_1^{n,k}, \dots, \phi_{a_{n,k}}^{n,k}\}$. Then $D_k^n \cup C_k^n$ form an orthonormal set.*

Proof. This follows from the fact that \mathbf{V} is a unitary matrix and from the choice of coefficients from equation (3). \square

For every cell $B_k^n \in \mathcal{B}^n$ in the tree T at level n , the SVD orthogonalization process is repeated. Let \mathcal{D}^n be the collection of orthonormal basis functions such that $\mathcal{D}^n = \cup_{B_k^n \in \mathcal{B}^n} D_k^n$, and the multilevel space be defined as $\mathbf{W}_n := \text{span}_{D_k^n \in \mathcal{D}^n} \{D_k^n\}$.

Although C_k^n forms an orthonormal set, these functions are not in general orthogonal to V_0 . However, it is clear that $\cup_{B_k^n \in \mathcal{B}^n} C_k^n$ form an orthonormal set. The next step is to work up the tree. For any two sibling cells denoted as B_{left}^n and B_{right}^n and corresponding basis functions C_{left}^n and C_{right}^n at level n , let $\mathcal{E}_k^{n-1} := C_{\text{left}}^n \cup C_{\text{right}}^n$ for some index k and let B_k^{n-1} be the corresponding cell at level \mathcal{B}^{n-1} . The orthogonalization process is repeated for the functions in \mathcal{E}_k^{n-1} . Rewrite the elements in \mathcal{E}_k^{n-1} as $\{\chi_1^{n-1}, \dots, \chi_{s_{n-1,k}}^{n-1}\}$ and form the set of equations

$$\begin{aligned} \phi_j^{n-1,k} &:= \sum_{i=1}^{s_{n-1,k}} c_{i,j}^{n-1,k} \chi_i^{n-1}, j \in \{1, \dots, a_{n-1,k}\}; \\ \psi_j^{n-1,k} &:= \sum_{i=1}^{s_{n-1,k}} d_{i,j}^{n-1,k} \chi_i^{n-1}, j \in \{a_{n-1,k} + 1, \dots, s_{n-1,k}\}. \end{aligned}$$

We can form the matrix

$$\mathbf{M}^{n-1,k} := \left[\begin{array}{ccc} (\phi_1(\mathbf{x}), \chi_1^{n-1}(\mathbf{x})) & \cdots & (\phi_1(\mathbf{x}), \chi_{s_{n-1,k}}^{n-1}(\mathbf{x})) \\ (\phi_2(\mathbf{x}), \chi_1^{n-1}(\mathbf{x})) & \cdots & (\phi_2(\mathbf{x}), \chi_{s_{n-1,k}}^{n-1}(\mathbf{x})) \\ \vdots & \vdots & \vdots \\ (\phi_M(\mathbf{x}), \chi_1^{n-1}(\mathbf{x})) & \cdots & (\phi_M(\mathbf{x}), \chi_{s_{n-1,k}}^{n-1}(\mathbf{x})) \end{array} \right]$$

and apply the SVD $\mathbf{M}^{n-1,k} = \mathbf{U}\mathbf{D}\mathbf{V}^T$. Suppose that $a_{n,k}$ is the rank of the matrix $\mathbf{M}^{n-1,k}$. Then under the choice

$$\left[\begin{array}{ccc|ccc} c_{1,1}^{n-1,k} & \cdots & c_{1,a_{n,k}}^{n-1,k} & d_{1,a_{n-1,k}+1}^{n-1,k} & \cdots & d_{1,s_{n-1,k}}^{n-1,k} \\ c_{2,1}^{n-1,k} & \cdots & c_{2,a_{n,k}}^{n-1,k} & d_{2,a_{n-1,k}+1}^{n-1,k} & \cdots & d_{2,s_{n-1,k}}^{n-1,k} \\ \vdots & \vdots & \vdots & \vdots & \vdots & \vdots \\ c_{s_{n-1,k},1}^{n-1,k} & \cdots & c_{s_{n-1,k},a_{n,k}}^{n-1,k} & d_{s_{n-1,k},a_{n-1,k}+1}^{n-1,k} & \cdots & d_{s_{n-1,k},s_{n-1,k}}^{n-1,k} \end{array} \right] := \mathbf{V},$$

for $i = 1, \dots, M$ and $j = a_{n-1,k} + 1, \dots, s_{n-1,k}$ we have that $\int_U \phi_i(\mathbf{x})^T \psi_j^{n-1,k}(\mathbf{x}) d\mathbf{x} = 0$.

For every cell $B_k^{n-1} \in \mathcal{B}^n$ in the tree T at level $n-1$ the SVD orthogonalization process is repeated. Let \mathcal{D}^{n-1} be the collection of orthonormal basis functions such that $\mathcal{D}^{n-1} = \cup_{B_k^{n-1} \in \mathcal{B}} D_k^{n-1}$ and the multilevel space be defined as $\mathbf{W}_{n-1} := \text{span}_{D_k^{n-1} \in \mathcal{D}^{n-1}} \{D_k^{n-1}\}$.

For any two sibling cells denoted as B_{left}^{n-1} and B_{right}^{n-1} and corresponding basis functions C_{left}^{n-1} and C_{right}^{n-1} at level n , let $\mathcal{E}_k^{n-2} := C_{\text{left}}^{n-1} \cup C_{\text{right}}^{n-1}$ for some index k and let B_k^{n-2} be the corresponding cell at level \mathcal{B}^{n-2} . It is clear that \mathcal{E}_k^{n-2} is an orthonormal set. The orthogonalization process is repeated for all the levels of the tree until the level 0 is reached. It is not hard to show that this process will terminate in at most $\mathcal{O}(nN)$ steps. Thus we have proved

Theorem 3.8. *Decompose \mathbf{V}_{n+1} as $\mathbf{V}_{n+1} \rightarrow \mathbf{V}_0 \oplus \mathbf{W}_0 \oplus \dots \mathbf{W}_n$ and*

- (i) *The complexity cost of the multi-level basis is bounded by $\mathcal{O}(nN)$.*
- (ii) *The multi-level basis vectors of $\mathbf{V}_0 \oplus \mathbf{W}_0 \oplus \dots \mathbf{W}_n$ form an orthonormal set.*

These multilevel basis functions can now be used to detect the anomaly $\mathbf{w}(\mathbf{x}, \omega)$ at the various levels of resolution.

3.1. Multilevel Detection.

Lemma 3.9. *Suppose that $\mathbf{v} \in L^2_{\mathbb{P}}(\Omega; L^2(U; \mathbb{R}^q))$ with KL expansion $\mathbf{v} = \sum_{p \in \mathbb{N}} \lambda_p^{\frac{1}{2}} \phi_p(\mathbf{x}) Y_p(\omega)$. Then for all $l \in \mathbb{N}_0$, $B_p^l \in \mathcal{B}^l$ and for the associated orthogonal projection coefficients $d_p^{l,k}(\omega) = \int_U \mathbf{v}^T \psi_p^{l,k} d\mathbf{x}$ we have that $\mathbb{E}[d_p^{l,k}] = 0$ and $\mathbb{E}[(d_p^{l,k})^2] \leq \sum_{i \geq M+1} \lambda_i$.*

Proof. The proof is a simple extension of the argument given in [9]. \square

As M increases, not only is the approximation error of the KL expansion reduced and dominated by the sum of eigenvalues, but the variance of the coefficients $d_p^{l,k}$ for the corresponding cell B_k^l is also controlled by the same quantity. We shall use this property to construct a reliable hypothesis test for detection of anomalous signals in any of the cells $B_k^l \in \mathcal{B}^l$ for $l = 0, \dots, n$.

Theorem 3.10 (Detection: Hypothesis Test). *Suppose that $\mathbf{u}(\mathbf{x}, \omega) = \mathbf{v}(\mathbf{x}, \omega) + \mathbf{w}(\mathbf{x}, \omega)$ and*

$$H_0 : \mathbf{u}(\mathbf{x}, \omega) = \mathbf{v}(\mathbf{x}, \omega) \quad H_A : \mathbf{u}(\mathbf{x}, \omega) \neq \mathbf{v}(\mathbf{x}, \omega).$$

Let $1 \geq \alpha \geq 0$ be the significance level. Then if the null hypothesis H_0 is true it follows that

$$\mathbb{P}(|d_p^{l,k}(\omega)| \geq \alpha^{-\frac{1}{2}} \sum_{i \geq M+1} \lambda_i) \leq \alpha.$$

Proof. The result follows from Lemma 3.9 and the Chebyshev inequality. \square

Remark. (Important) With this hypothesis test the coefficients $d_p^{l,k}$ can be used as detectors of anomalous signals in the cell B_k^l . Here are the key features of this detector:

- Decay of the eigenvalues with M controlling the sharpness of the bound.
- For validity of the hypothesis test only a good estimate of the covariance function is needed.

- **No assumptions on independence nor underlying distribution (e.g. Normal, Poisson, etc.) of the data.**

An alternative approach for detecting signals is to measure the size of the anomaly with respect to a suitable norm.

Theorem 3.11. *Suppose that $\mathbf{u}(\mathbf{x}, \omega) = \mathbf{v}_M(\mathbf{x}, \omega) + \mathbf{w}(\mathbf{x}, \omega)$ for some $\mathbf{w}(\mathbf{x}, \omega) \in L^2_{\mathbb{P}}(\Omega; L^2(U; \mathbb{R}^q))$, where $\mathbf{w}(\mathbf{x}, \cdot) \in \mathbf{V}_0^\perp \cap \mathbf{V}_{n+1}$ almost surely. Then*

$$\begin{aligned} \sum_{l=0}^n \sum_{\psi_p^{l,k} \in D_k^l} \sum_{D_k^l \in \mathcal{D}^l} (d_p^{l,k})^2 &= \|\mathbf{w}(\mathbf{x}, \omega)\|_{L^2(U; \mathbb{R}^q)}^2 \quad (a.s.) \text{ and} \\ \sum_{l=0}^n \sum_{\psi_p^{l,k} \in D_k^l} \sum_{D_k^l \in \mathcal{D}^l} \mathbb{E} \left[(d_p^{l,k})^2 \right] &= \|\mathbf{w}\|_{L^2_{\mathbb{P}}(\Omega; L^2(U; \mathbb{R}^q))}^2. \end{aligned}$$

Proof. The result follows from the orthogonality of the multilevel basis of $\mathbf{W}_0 \oplus \dots \mathbf{W}_n$. □

Thus under the model $\mathbf{u}(\mathbf{x}, \omega) = \mathbf{v}_M(\mathbf{x}, \omega) + \mathbf{w}(\mathbf{x}, \omega)$ the size of the anomaly for $\mathbf{w}(\mathbf{x}, \omega)$ can be calculated from the projection coefficients of the basis functions in $\mathbf{V}_0^\perp \cap \mathbf{V}_{n+1} = \mathbf{W}_0 \oplus \dots \mathbf{W}_n$.

In many cases the nominal behavior of the signal cannot be captured assuming a finite dimensional random field $\mathbf{v}_M(\mathbf{x}, \omega)$. Suppose that $\mathbf{u}(\mathbf{x}, \omega) = \mathbf{v}(\mathbf{x}, \omega) + \mathbf{w}(\mathbf{x}, \omega)$, but $\mathbf{w}(\mathbf{x}, \cdot) \in \mathbf{V}_0^\perp \cap \mathbf{V}_{n+1}$ almost surely. In this case the tail of the KL expansion of $\mathbf{v}(\mathbf{x}, \omega)$ intersects with the anomaly. However, the size of the anomaly can still be bounded.

Theorem 3.12. *Let $t_M := \sum_{j \geq M+1} \lambda_j$, $s_M := \sum_{j \geq M+1} \sqrt{\lambda_j}$, and suppose that $\mathbf{u}(\mathbf{x}, \omega) = \mathbf{v}(\mathbf{x}, \omega) + \mathbf{w}(\mathbf{x}, \omega)$ for some $\mathbf{w}(\mathbf{x}, \omega) \in L^2_{\mathbb{P}}(\Omega; L^2(U; \mathbb{R}^q))$, where $\mathbf{w}(\mathbf{x}, \cdot) \in \mathbf{V}_0^\perp \cap \mathbf{V}_{n+1}$ almost surely. Then*

$$\begin{aligned} \|\mathbf{w}\|_{L^2_{\mathbb{P}}(\Omega; L^2(U; \mathbb{R}^q))}^2 (1 - 2s_M) + t_M &\leq \sum_{l=0}^n \sum_{\psi_p^{l,k} \in D_k^l} \sum_{D_k^l \in \mathcal{D}^l} \mathbb{E} \left[(d_p^{l,k})^2 \right] \\ &\leq \|\mathbf{w}\|_{L^2_{\mathbb{P}}(\Omega; L^2(U; \mathbb{R}^q))}^2 (1 + 2s_M) + t_M. \end{aligned}$$

Proof. The result is a simple extension of the proof of Theorem 3 in [9]. □

4. APPLICATION: DEFORESTATION AND FOREST DEGRADATION

This mathematical framework is well suited for detecting changes in terrestrial land surfaces based on both optical and radar data. The mathematical framework is applied to data collected from the Sentinel-2 and Landsat satellites for the detection of forest degradation in the Amazon. Detection here is a complex task, as can be seen from Figure 4. In particular, detection of changes in the state of a forest are significantly hindered by the presence of misleading anomaly artefacts such as cloud cover. We first demonstrate the application of this multilevel anomaly filter to Landsat satellite optical sensor data [45, 54]. The Enhanced Vegetation Index (EVI) [27] is a benchmark quantity calculated from satellite measurements, with an important goal of detecting forest degradation. In this test example we extract a slice sized at 25×18 pixels.

Remark. A cloud masking detection algorithm is applied [58]. These algorithms are not perfect, and in many instances clouds fail to be detected or removed (see Figure 4). The approach developed above provides a much more viable mechanism for automatically detecting and accounting for these cloud artefacts.

Each pixel corresponds to a $30m \times 30m$ patch of land. With a starting date of June 2016, 95 terrain slices (frame numbers 1 to 95) are collected. A covariance function is constructed from the first 65 time slices (through to day 1288). The KL expansion eigenspaces are computed and the multilevel filter is constructed with $M = 40$. The probabilities under the null hypothesis test $H_0 : \mathbf{u}(\mathbf{x}, \omega) = \mathbf{v}(\mathbf{x}, \omega)$ for coefficients $d_p^{l,k}(\omega)$ are given by $\mathbb{P}(|d_p^{l,k}(\omega)| \geq \alpha^{-\frac{1}{2}} \sum_{i \geq M+1} \lambda_i) \leq \alpha$,

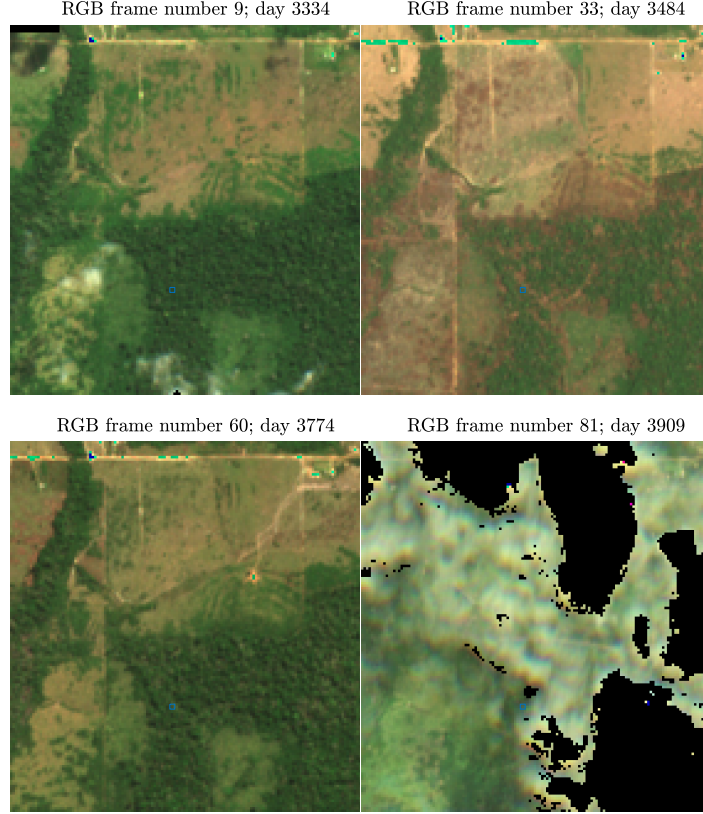


FIGURE 4. Deforestation sequence from Sentinel 2 satellite data. Four frames of Amazon forest at *days* 3335, 3484, 3774 and 3909 showing the clearing and regrowth of forest. Coordinate pixel at (108,66) is marked with a small blue box. Note that from the brown discoloration at *day* 3484 swaths of the trees are cleared. By *day* 3774 the forest vegetation grows back from nearby trees. However, as we will see, it does not return to the earlier state, as this is new forest. This will be clear when we apply the multilevel filter to the EVI data. However, it will be significantly more pronounced within the multispectral data. Frame (81) corresponds to a cloudy day in which the standard cloud removal algorithm fails. The multilevel filter provides a tool to recognize these data as a false anomaly by analysis of the time sequence.

where α is the significance level. It is assumed that λ_M dominates the infinite sum $\sum_{k=M+1}^{\infty} \lambda_k$. This assumption is made due to limitations on availability of data as well as the rapid decay of the eigenvalues. The multilevel filter is applied to each frame number starting from 66 (day 1304).

The projection coefficients d_l^k are computed for levels $l = 0, \dots, 3$ for each available *day* e.g. $W_0^{day}, W_1^{day}, \dots, W_3^{day}$. The contribution to the total size of the anomaly $\|\mathbf{w}(\mathbf{x})\|_{L^2(U; \mathbb{R}^q)}$ for any fixed realization on *day*, within each cell B_k^l , is computed as $E_p^{l,k} := \sqrt{\sum_{\psi_p^{l,k} \in D_k^l} (d_p^{l,k})^2}$. Note that for any fixed *day* if $\mathbf{w}(\mathbf{x}, \cdot) \in \mathbf{V}_0^\perp \cap \mathbf{V}_{n+1}$ then a.s. $\|\mathbf{w}(\mathbf{x}, \omega)\|_{L^2(U; \mathbb{R}^q)}^2 = \sum_{l=0}^n \sum_{\psi_p^{l,k} \in D_k^l} \sum_{D_k^l \in \mathcal{D}^l} (d_p^{l,k})^2$.

In Figure 5, corresponding to day 1304, there is an image of the forest featuring a small patch of bare ground on the upper right corner. Until day 1304 the vegetation of the terrain has not changed, so that we expect small anomaly measurements. The cells $B_p^{l,k}$ and levels of resolution $l = 0, \dots, 3$ are overlaid on the RGB image with different semi-transparent colors. The structure of the forest can be seen. The spatial intensities of the stochastic anomalies for levels $l = 0, \dots, 3$ are

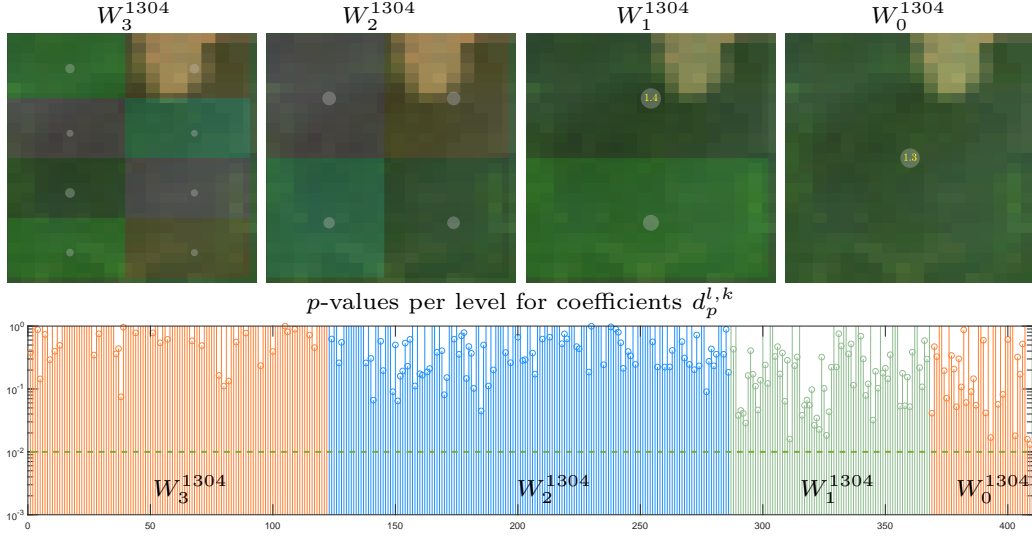


FIGURE 5. Multilevel anomaly map for day 1304 (small anomalies). There are very few statistical changes relative to the training data set of the multilevel filter. The top image corresponds to the multilevel cells $B_k^l \in \mathcal{B}^l$ on the patch of terrain for each level $l = 0, 1, \dots, 3$ overlain on the RGB map from the Landsat optical measurements. The corresponding multilevel spaces $W_3^{1304}, \dots, W_0^{1304}$ are given for day 1304 and level l . To indicate that the data is scalar we use the unbolded characters. The bottom figure corresponds to the probability for each coefficient $d_p^{l,k}$ with respect to level of resolutions $l = 0, 1, \dots, 3$. The cell supports for each level of resolution are traced by the points of different colors. Notice that the cell size is smaller for higher levels and larger for lower levels. The grey circle in the middle of the cell B_k^l reflects the size of anomaly given by $E_p^{l,k} := \left(\sum_{\psi_p^{l,k} \in D_k^l} (d_p^{l,k})^2 \right)^{\frac{1}{2}}$ for each cell $B_k^l \in \mathcal{B}^l$; we can see these are small. For anomalies greater than 1, the size of the anomaly is printed in yellow text. This is also reflected in the probability per level (based on hypothesis tests) of each coefficient $d_p^{l,k}$. Note that the magnitudes of the anomalies per cell are small. Furthermore, there are no null hypothesis tests with probability below the significance level $\alpha = 10^{-2}$ (dashed line).

small. This is also reflected in the tests of the null hypothesis H_0 for the test statistic coefficients $d_p^{l,k}$, where the p -values are larger than the significance level $\alpha = 10^{-2}$.

In Figure 6 (a) we observe that for day 1336 many anomalies are detected for the cells $B_p^{l,k}$. This can be seen from the jump in intensities of the measured anomaly magnitudes $E_p^{l,k}$ and corresponding sizes of the grey disks. Furthermore, the p values of the test of the null hypothesis H_0 are below the significance level of $\alpha = 10^{-2}$. This is consistent with the visual changes that are observed on RGB image, where it is seen that parts of the forest are removed and more bare ground is observed. In Figure 6 (b), day 1352, it is observed that additional trees have been removed. This is reflected in the larger anomaly measurements seen in the cells $B_p^{l,k}$ and the corresponding hypothesis tests.

4.1. Anomaly sequence on Sentinel 2 scalar data. We now focus on the multilevel filter output from a series of Sentinel 2 optical sensor data [18], and on the change in the anomaly as time evolves (Figure 4). This example illustrates the complexity of degradation as the detected logging of the forest on day 3484 does not notably change the land cover, which remains forest. Further, the forest

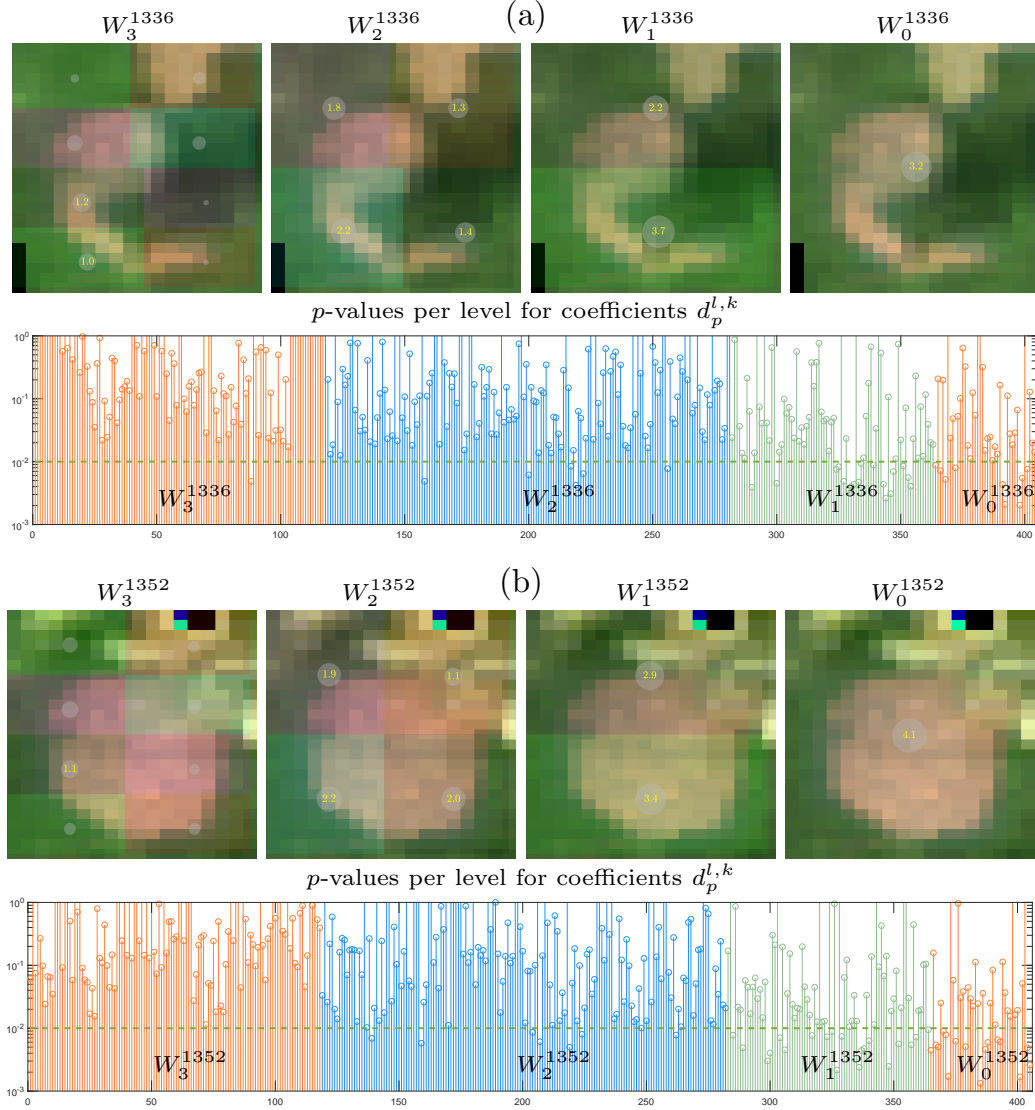


FIGURE 6. Multilevel anomaly map for day 1336 (large changes). In contrast to day 1304 we observe changes in large regions of the forest. This is reflected in the magnitude of $E_p^{l,k}$ in each cell B_k^l and from the corresponding hypothesis tests. We observe that at level $l = 2$ many p -values of the coefficients d_l^k are below the significance level 10^{-2} . This becomes more pronounced for levels $l = 1$ and $l = 0$.

does not stay in a degraded state and is allowed to recover. Note that the anomaly introduced by imperfect cloud masking on day 3909 significantly complicates the task of detecting changes in the forest. As for the case of Landsat data, we compute the EVI from the optical spectral data. From 71 Sentinel 2 data frames starting from day 1 to day 3200 the covariance structure is analyzed and the multilevel anomaly filter is implemented. Each pixel of the 150×150 area corresponds to a land patch of $10m \times 10m$. We further extract 75×75 landcover, construct the multilevel filter with $M = 51$ and apply the multilevel filter to each of the EVI test frames starting from day 3300 (corresponding to frame number 1). Given the assumption that $\mathbf{w}(\mathbf{x}, \cdot) \in \mathbf{V}_0^\perp \cap \mathbf{V}_{n+1}$ an anomaly map is reconstructed as $\mathbf{w}(\mathbf{x}, \omega) = \sum_{l=0}^n \sum_{\psi_p^{l,k} \in D_k^l} \sum_{D_k^l \in \mathcal{D}^l} d_p^{l,k} \psi_p^{l,k}(\mathbf{x})$. Further it

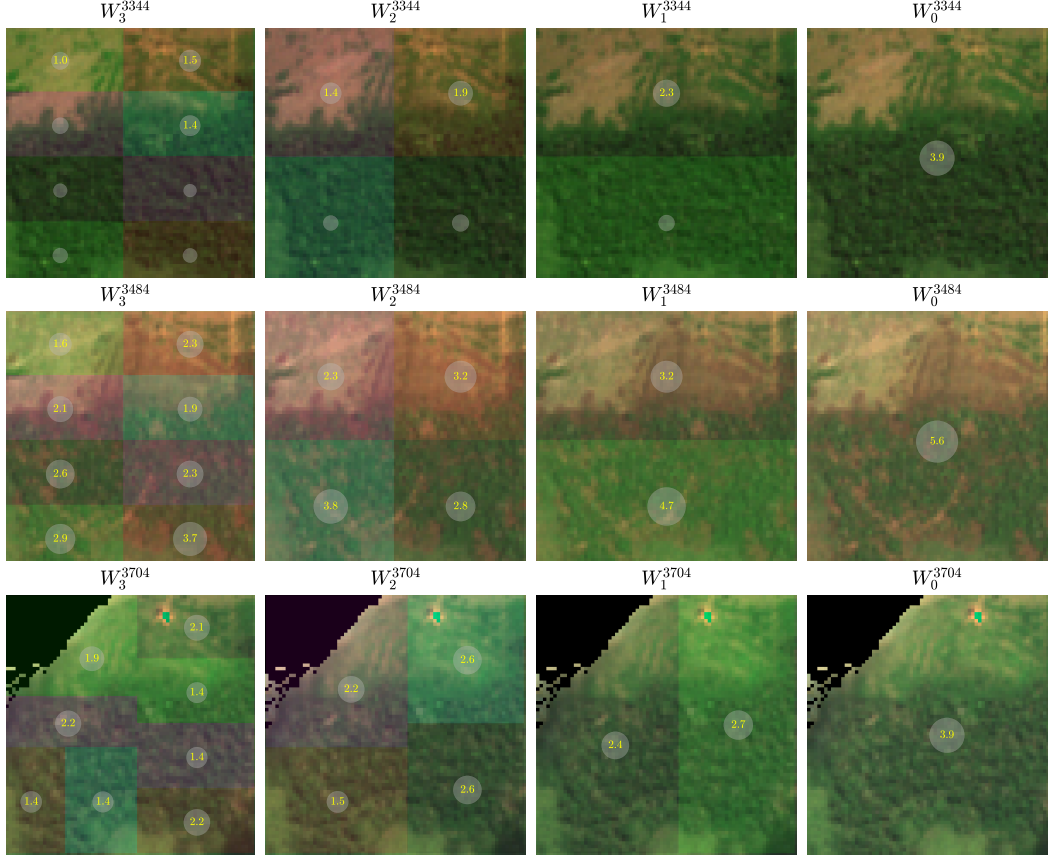


FIGURE 7. Multilevel projection coefficient anomaly map for scalar EVI Sentinel 2 data on a 75×75 land cover patch for days 3344, 3484 and 3704. For *day* 3344 the sizes of the anomalies $E_p^{l,k}$ are shown for each cell $B_p^{l,k}$. On *day* 3484 a part of the tree cover in the forest is removed, so that magnitudes of the anomalies increase. By *day* 3704 the forest has largely recovered, but sizes of the anomalies are still somewhat larger than for *day* 3344. This is due to the new vegetation. As will be observed, these changes will be significantly more pronounced for multilevel anomaly detection on the multispectral Sentinel 2 data. Note that sizes of the cells change due to missing data caused by cloud cover.

can be shown that if the null hypothesis holds then for each pixel the anomaly map satisfies $\mathbb{P}(|\int_{\tilde{U}} \mathbf{w}(\mathbf{x}, \omega) d\mathbf{x}| \geq \alpha^{-\frac{1}{2}} \sum_{i \geq M+1} \lambda_i \int_{\tilde{U}} \phi_i^2(\mathbf{x}) d\mathbf{x}) \leq \alpha$ for any region $\tilde{U} \subset U$ around the pixel.

From Figure 4 note that many of the trees are removed but regrow back with time. The last image corresponds to a cloudy day on which the cloud removal algorithm has trouble detecting clouds and only a subset are removed (black pixels). As seen above, for deforestation tracking algorithms distinguishing forest changes from cloud cover is a challenge.

In Figure 7 the multilevel anomaly map for *day* 3344, 3484 and 3704 are shown for levels of resolution $l = 0, \dots, 3$. In Figure 8 the corresponding p -values for are displayed for each coefficient $d_p^{l,k}$ for the same sequence of days. We observe that for *day* 3344 the anomalies are small and concentrated on the top of the image outside of the forest. This is reflected in the hypothesis tests, where almost all the p -values are above the significance level of $\alpha = 0.05$. On *day* 3484 deforestation appears and as expected, with the anomaly metrics $E_p^{l,k}$ significantly increasing and the p -values for many of the coefficients becoming significant. On *day* 3704 regrowth from adjacent trees covers

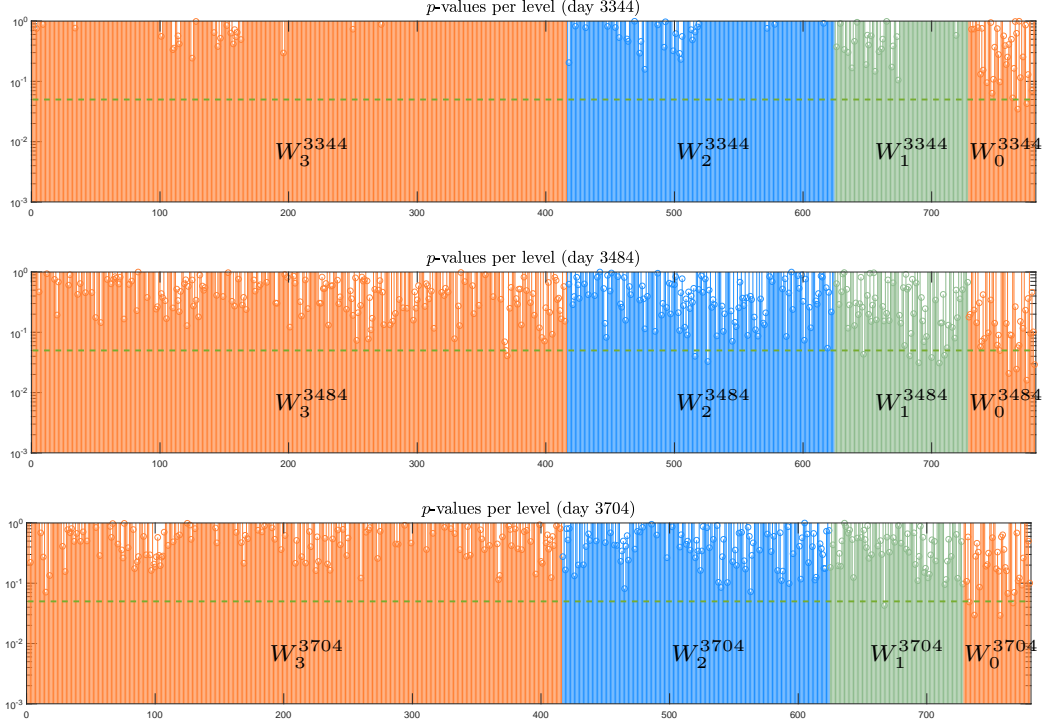


FIGURE 8. Multilevel coefficient probabilities for scalar EVI Sentinel 2 data for days 3344, 3484 and 3704. For *day* 3344 the p -values of the hypothesis test for each coefficient are largely above the significance level of $\alpha = 0.05$. This is consistent with Figure 7 for the same day. On *day* 3484 part of the tree cover in the forest is removed, and p -values drop significantly. On *day* 3704 the forest has mostly recovered, but not entirely to its original state.

the bare ground. The anomalies reduce and the p -values are less significant. However, notice that it is still more significant than for *day* 3344. This is due to new vegetation that is partly captured with the EVI index. As will be seen, with the application of the multilevel vector field method on the multilevel spectral data, this will be substantially more pronounced.

In Figure 9 (a) the anomaly for pixel coordinate (108,66) is tracked in time. A robust LOESS [34] is applied to the anomaly sequence. On *day* 3499 we note the large jump in the anomaly for that pixel coordinate, due to the removal of trees. As time evolves the anomaly metric grows, reflecting the clearing of trees. However, the vegetation from nearby trees grows into the area (*day* 3774), and eventually the anomaly level returns to zero. This is expected as leaves in the forest age. On the cloudy *day* (3909), the anomaly is ignored from the LOESS regression as it is recognized as an outlier, with similar behavior at other pixel locations with cloud cover.

Remark. (Important) From the direct EVI measurements in Figure 9 (b) at pixel (108,66), it is not possible to distinguish cloud cover from vegetation at the anomaly circled in red. Current methods that directly use the EVI measurements will be blind to this type of problem. In particular, the cloud masking algorithm developed in [58] was unable to properly classify the cloud cover, potentially leading to erroneous pictures of the forest state. Using the anomaly filter, cloud cover can be more easily identified – development of a cloud identification algorithm is being explored in detail.

Remark. (Important) One feature of this approach is its augmentation of current statistical methods to better characterize the signal in time. For example, applying the robust LOESS we can more

easily identify clouds. Similar advantages have been observed in the anomalous sequences for change points, where it becomes clearer how and where the stochastic properties of the signal differ in time. This means that we can apply current change point detection algorithms to these anomalous signals. This will be further investigated in a later publication.

4.2. Anomaly sequences on multimodal vector field data ($q = 6$). Results are shown below for application of the multilevel filter to vector field data. From the Sentinel 2 dataset used in the previous experiment, the same landcover of 75×75 pixels is extracted. However, here we do not compute the EVI index from individual optical bands but instead use all of the optical bands 1 - 6 (blue, green, red, near-infrared, shortwave infrared 1 and shortwave infrared 2) as a vector field defined on the land cover. The covariance functional matrix across all bands is estimated and the eigenspace is constructed for $M = 51$ eigenfunctions. The anomaly sequence is computed from the vectorial field multilevel filter $\mathbf{w}(\mathbf{x}, \omega) = \sum_{l=0}^n \sum_{\psi_p^{l,k} \in D_k^l} \sum_{D_k^l \in \mathcal{D}^l} d_p^{l,k} \psi_p^{l,k}(\mathbf{x})$ for each available *day*.

It is advantageous to study forest degradation by incorporating all correlations of the anomalies across spatial and band data. In Figure 10 sizes of anomalies for days 3344, 3484 and 3704 are shown. Due to scaling of the data, anomalies are divided by 1000 and colored yellow if they are larger than 3. For *day* 3344 sizes of anomalies $E_p^{l,k}$ are shown for each cell $B_p^{l,k}$. Anomalies are relatively small, as only the grasslands present the largest changes in vegetation. On *day* 3484 part of the tree cover is removed, and sizes of the anomalies increase significantly. This is consistent with the scalar EVI anomaly map shown in Figure 7. On *day* 3704 the forest has essentially recovered, but in contrast to the scalar EVI, data sizes of anomalies increase further. This is due to the near-infrared (band 4) spectral data that reflect new chlorophyll from forest regrowth. This is consistent with Figure 11 where the anomaly signaled by the near-infrared band increases significantly at *day* 3704.

In Figure 11 the anomaly time sequences for all 6 bands are shown for pixel (96,70). From the RGB bands (1-3) observe the relation of the clearing of trees by day 3484 to increases in the anomaly levels for all 3 bands. In addition, particularly in band 4 (near infrared), by *day* 3600 the anomaly becomes more notable. Near infrared as a modality detects new leaves (chlorophyll). This is observable with the growth of vegetation after the clearing of some of the trees around day 3484. By the last day the anomaly level in near infrared slowly decreases, consistent with aging of the leaves.

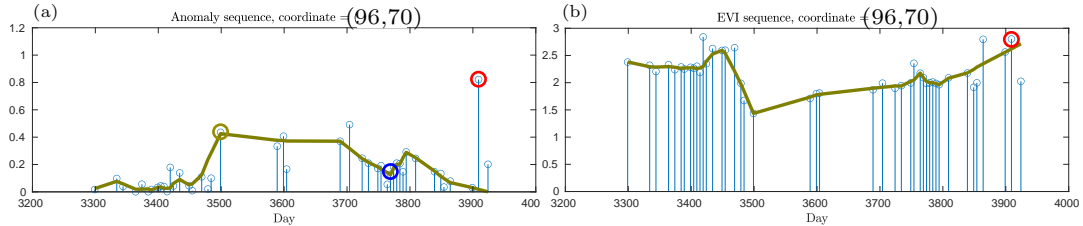


FIGURE 9. Anomaly sequence in a pixel-level time series of satellite data mapping environmental change illustrated in Figure 4. The multilevel anomaly filter is applied spatially to each frame, with the anomaly quantified and plotted against time. A robust LOESS is performed on the sequence (olive line). (a) Logging of the forest is detected on day 3484, where anomaly level increases. After logging, the forest is allowed to recover, with recovery determined on day 3774 (blue circle). On day 3909 (red circle) a localized anomaly is caused by cloud screening (image on day 3909 in Figure 4), but the LOESS filter effectively ignores this false anomaly. (b) In contrast, on day 3909 in the direct EVI sequence cannot indicate if the change is due to a cloud or vegetation, as they have almost the same measurable outputs.

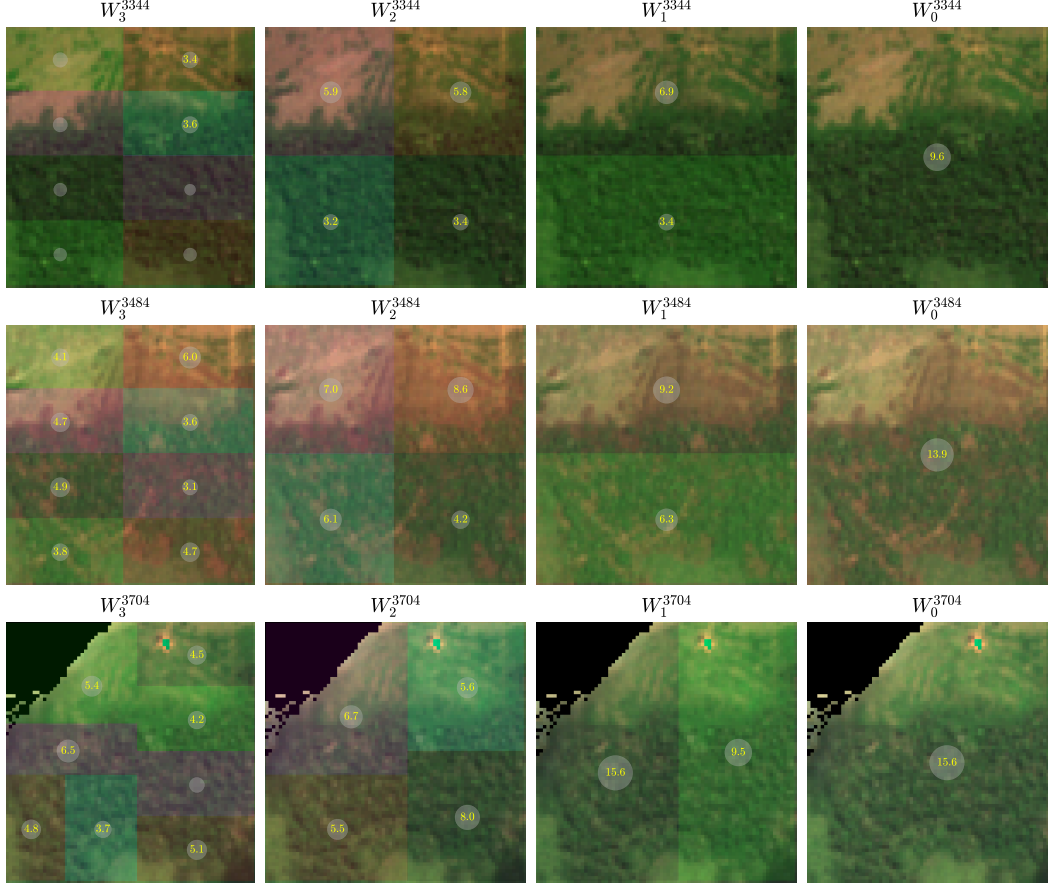


FIGURE 10. Multilevel projection coefficient anomaly map for vector field Sentinel 2 data on a 75×75 landcover patch for days 3344, 3484 and 3704. Six spectral bands are used that include blue, green, red, near-infrared, shortwave infrared 1 and shortwave infrared 2. For visualization purposes the anomaly sizes are divided by 1000 and only printed in yellow if they are greater than 3. For *day* 3344 the size of the anomalies $E_p^{l,k}$ are shown for each cell $B_p^{l,k}$. On *day* 3484 part of the trees in the forest are removed and thus the size of the anomalies increase significantly. On *day* 3704 the forest has mostly recovered, but in contrast to the scalar EVI data from Figure 7 the size of the anomalies further increase. This is due to the near-infrared (band 4) spectral data which detects new chlorophyll. This is consistent with Figure 11 where the anomaly of band 4 increases significantly at *day* 3704.

Remark. Note that we did not present explicit hypothesis tests for this example, which would have required a larger order for filter M , to capture a smaller eigenvalues. The data are insufficient to produce the required eigenspaces. However, sizes of projection coefficients can still be used to quantify the anomalies.

5. CONCLUSIONS

In this paper we have developed a multilevel basis that is adapted to the truncated Karhunen-Loève expansion of a nominal random vector field. We show a full rigorous proof of the existence and optimality of the KL expansion for random vector fields. Numerical construction of the multilevel basis for the vector field is achieved with an efficient algorithm originating in the numerical solution

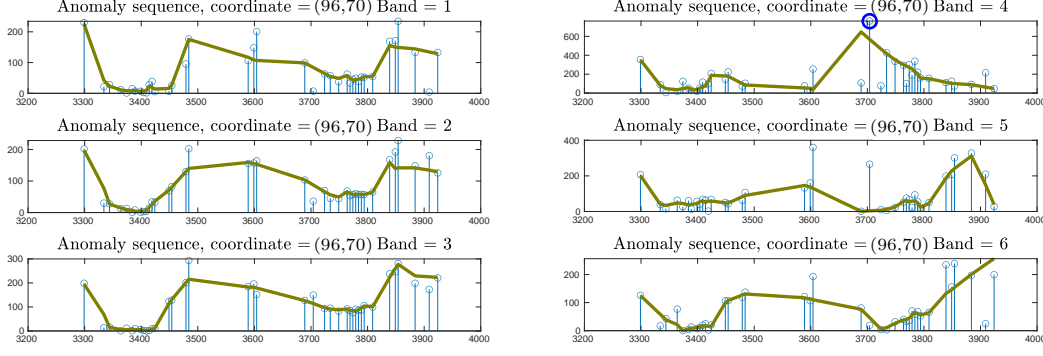


FIGURE 11. Deforestation anomaly sequence for multi modality Sentinel 2 data. Anomalies are detected with respect to all bands. By *day* 3484 the clearing of the trees are captured by the anomaly increase of bands 1 - 3 (RGB). As the tree grow back the anomalies are slowly reduced. However, around *day* 3704 the anomaly of the near-infrared band peaks. The clearing of the trees in parts of the forest eventually leads to regrowth of the forest with new leaves. The near-infrared band is used to detect the presence of new chlorophyll in the leaves. Notice that the anomaly for this band peaks at *day* 3704 (see the blue circle). This is consistent with the regrowth.

of PDEs. Detection is achieved by examining relative contributions to the multilevel spaces. Anomalies are quantified using a suitable norm and reliable hypothesis tests with weak assumptions. We apply our approach to the problem of deforestation and degradation in the Amazon forest. This approach does not replace, but rather augments current statistical approaches. For example, the multilevel filter amplitudes can signal anomalous behavior that can be tracked through identifiable transitions using change point detection methods. Furthermore, these anomalous behaviors can be identified at multiple change points, further elucidating temporal behaviors. We are currently further investigating these latter aspects.

Another problem of very general interest in this area is the reliable identification of cloud cover. We have demonstrated a more effective approach to this problem by examining variable temporal behavior anomalies. We are currently developing a fuller algorithm to achieve this.

APPENDIX

PROOF OF PROPOSITION 2.2

Proof. First we show that $\{\mathbf{v}_k(\mathbf{x})\mathbf{v}_l(\mathbf{y})^T\}_{k,l \in \mathbb{N}}$ are orthonormal. Note

$$\begin{aligned}
 (\mathbf{v}_i(\mathbf{x})\mathbf{v}_j(\mathbf{y})^T, \mathbf{v}_k(\mathbf{x})\mathbf{v}_l(\mathbf{y})^T)_{L^2(U; \mathbb{R}^{q \times q})} &= \int_U \int_U \mathbf{1}^T (\mathbf{v}_i(\mathbf{x})\mathbf{v}_j(\mathbf{y})^T \bullet \mathbf{v}_k(\mathbf{x})\mathbf{v}_l(\mathbf{y})^T) \mathbf{1} \, d\mathbf{x} d\mathbf{y} \\
 (4) \quad &= \int_U \int_U \mathbf{1}^T \begin{bmatrix} v_1^i(\mathbf{x})v_1^k(\mathbf{x}) \\ v_2^i(\mathbf{x})v_2^k(\mathbf{x}) \\ \vdots \\ v_q^i(\mathbf{x})v_q^k(\mathbf{x}) \end{bmatrix} \begin{bmatrix} v_1^j(\mathbf{y})v_1^l(\mathbf{y}) & \dots & v_q^j(\mathbf{y})v_q^l(\mathbf{y}) \end{bmatrix} \mathbf{1} \, d\mathbf{x} d\mathbf{y} \\
 &= \int_U \mathbf{v}_i(\mathbf{x})^T \mathbf{v}_k(\mathbf{x}) \, d\mathbf{x} \int_U \mathbf{v}_j(\mathbf{y})^T \mathbf{v}_l(\mathbf{y}) \, d\mathbf{y} = \delta[i - k] \delta[j - l].
 \end{aligned}$$

Let $\mathbf{F} \in L^2(U \times U; \mathbb{R}^{q \times q})$ and suppose that

$$\int_U \int_U \mathbf{1}^T(\mathbf{F}(\mathbf{x}, \mathbf{y}) \bullet \mathbf{v}_k(\mathbf{x}) \mathbf{v}_l(\mathbf{y})) \mathbf{1} \, d\mathbf{x} d\mathbf{y} = 0$$

for all $k, l \in \mathbb{N}$. Then

$$\begin{aligned} \int_U \int_U \mathbf{1}^T(\mathbf{F}(\mathbf{x}, \mathbf{y}) \bullet \mathbf{v}_k(\mathbf{x}) \mathbf{v}_l(\mathbf{y})) \mathbf{1} \, d\mathbf{x} d\mathbf{y} &= \int_U \int_U \sum_{i,j} F_{i,j}(\mathbf{x}, \mathbf{y}) v_i^k(\mathbf{x}) v_j^l(\mathbf{y}) \, d\mathbf{x} d\mathbf{y} \\ (5) \quad &= \int_U \sum_{j=1}^q v_j^l(\mathbf{y}) \left(\int_U \sum_{i=1}^q F_{i,j}(\mathbf{x}, \mathbf{y}) v_i^k(\mathbf{x}) \, d\mathbf{x} \right) d\mathbf{y} = 0 \end{aligned}$$

Since $\{\mathbf{v}_l\}_{l \in \mathbb{N}}$ is a complete orthonormal basis of $L^2(U; \mathbb{R}^q)$, it follows

$$(6) \quad \int_U \sum_{i=1}^q F_{i,j}(\mathbf{x}, \mathbf{y}) v_i^k(\mathbf{x}) \, d\mathbf{x} = 0$$

almost everywhere for all $k \in \mathbb{N}$. Now, for each $k \in \mathbb{N}$ let D_k be the set of measure zero on which (6) does not hold. Letting $D := \cup_{k \in \mathbb{N}} D_k$, if $\mathbf{y} \notin D$ then

$$\int_U \sum_{i=1}^q F_{i,j}(\mathbf{x}, \mathbf{y}) v_i^k(\mathbf{x}) \, d\mathbf{x} = 0$$

for all $k \in \mathbb{N}$. Since $\{\mathbf{v}_k\}_{k \in \mathbb{N}}$ is a complete orthonormal basis for $L^2(U; \mathbb{R}^q)$ it follows $\mathbf{F}(\mathbf{x}, \mathbf{y}) = \mathbf{0}$ almost everywhere with respect to the measure $d\mathbf{x} d\mathbf{y}$. \square

PROOF OF PROPOSITION 2.3

Proof. From Proposition 1 we have that $\{\mathbf{v}_k \mathbf{v}_l^T\}_{k,l \in \mathbb{N}}$ is a complete orthonormal basis for $L^2(U \times U; \mathbb{R}^{q \times q})$. Conversely, from Proposition 2 in [43] we have that $\{\mathbf{v}_k \otimes \mathbf{v}_l\}_{k,l \in \mathbb{N}}$ is a complete orthonormal basis for $L^2(U; \mathbb{R}^q) \otimes L^2(U; \mathbb{R}^q)$. Now define the map $\mathcal{M} : L^2(U; \mathbb{R}^q) \otimes L^2(U; \mathbb{R}^q) \rightarrow L^2(U \times U; \mathbb{R}^{q \times q})$ such that

$$\mathcal{M}(\mathbf{v}_k \otimes \mathbf{v}_l) = \mathbf{v}_k \mathbf{v}_l^T$$

for all $k, l \in \mathbb{N}$. Let $f \in L^2(U; \mathbb{R}^q) \otimes L^2(U; \mathbb{R}^q)$, so that we can write $f = \sum_{k,l} \alpha_{k,l} \mathbf{v}_k \otimes \mathbf{v}_l$. Define the map $\mathcal{M}' : L^2(U; \mathbb{R}^q) \otimes L^2(U; \mathbb{R}^q) \rightarrow L^2(U \times U; \mathbb{R}^{q \times q})$ as

$$\mathcal{M}' f = \sum_{k,l} \alpha_{k,l} \mathcal{M}(\mathbf{v}_k \otimes \mathbf{v}_l) = \sum_{k,l} \alpha_{k,l} \mathbf{v}_k \mathbf{v}_l^T.$$

We have that

$$(7) \quad (\mathcal{M}' f, \mathcal{M}' f)_{L^2(U \times U; \mathbb{R}^{q \times q})} = \sum_{k,l} \sum_{k',l'} \alpha_{k,l} \alpha_{k',l'} (\mathbf{v}_k \mathbf{v}_l^T, \mathbf{v}_{k'} \mathbf{v}_{l'}^T)_{L^2(U \times U; \mathbb{R}^{q \times q})} = \sum_{k,l} \alpha_{k,l}^2.$$

Conversely, we have

$$(f, f)_{L^2(U; \mathbb{R}^q) \otimes L^2(U; \mathbb{R}^q)} = \sum_{k,l} \sum_{k',l'} \alpha_{k,l} \alpha_{k',l'} (\mathbf{v}_k \otimes \mathbf{v}_l, \mathbf{v}_{k'} \otimes \mathbf{v}_{l'})_{L^2(U; \mathbb{R}^q) \otimes L^2(U; \mathbb{R}^q)} = \sum_{k,l} \alpha_{k,l}^2.$$

\square

PROOF OF PROPOSITION 2.4

Proof. This result follows from a similar argument as that for the proofs of Proposition 2.2 and 2.3. \square

ACKNOWLEDGMENTS

We appreciate the help from Pontus Olofsson, Hanfeng Gu and Xiaojing Tang in providing the Landsat and Sentinel-2 datasets. Furthermore, their expertise in remote sensing was useful in placing context to this work and in interpreting the results. We also appreciate the feedback from Sucharita Gopal. This material is based upon work supported by the National Science Foundation (and Department of Energy) under Grant No. 1736392.

REFERENCES

- [1] E. Arias-Castro, D. Donoho, and X. Huo. Near-optimal detection of geometric objects by fast multiscale methods. *IEEE Transactions on Information Theory*, 51:2402, 2005.
- [2] Ery Arias-Castro, Rui M. Castro, Ervin Tánzos, and Meng Wang. Distribution-free detection of structured anomalies: Permutation and rank-based scans. *Journal of the American Statistical Association*, 113(522):789–801, 2018.
- [3] A. Aue, S. Hörmann, L. Horváth, M. Hušková, and J. G. Steinebach. Sequential testing for the stability of high-frequency portfolio betas,. *Econometric Theory*, 28:804, 2012.
- [4] A. Aue and L. Horváth. Structural breaks in time series. *Journal of Time Series Analysis*, 34:1, 2013.
- [5] Matheus HC Barboza, Ricardo de S Alencar, Julio C Chaves, Moacyr AHB Silva, Romulo D Orrico, and Alexandre G Evsukoff. Identifying human mobility patterns in the rio de janeiro metropolitan area using call detail records. *Transportation Research Record*, page 0361198120977655, 2020.
- [6] J. E. Castrillón-Candás and K. Amaratunga. Fast estimation of continuous karhunen-loeve eigenfunctions using wavelets. *IEEE Transactions on Signal Processing*, 50(1):78–86, 2002.
- [7] J. E. Castrillón-Candás and Kevin Amaratunga. Spatially adapted multiwavelets and sparse representation of integral equations on general geometries. *SIAM Journal on Scientific Computing*, 24(5):1530–1566, 2003.
- [8] J. E. Castrillón-Candás, M. G. Genton, and R. Yokota. Multi-level restricted maximum likelihood covariance estimation and Kriging for large non-gridded spatial datasets. *Spatial Statistics*, 18, Part A:105 – 124, 2016. Spatial Statistics Avignon: Emerging Patterns.
- [9] Julio E. Castrillón-Candás and Mark Kon. Anomaly detection: A functional analysis perspective. *Journal of Multivariate Analysis*, 189:104885, 2022.
- [10] Julio Enrique Castrillón-Candás, Dingning Liu, and Mark Kon. Stochastic functional analysis with applications to robust machine learning, 2021. 10.48550/ARXIV.2110.01729.
- [11] F Stuart Chapin Iii, Erika S Zavaleta, Valerie T Eviner, Rosamond L Naylor, Peter M Vitousek, Heather L Reynolds, David U Hooper, Sandra Lavorel, Osvaldo E Sala, Sarah E Hobbie, et al. Consequences of changing biodiversity. *Nature*, 405(6783):234–242, 2000.
- [12] Yimin Chen, Xiaoping Liu, Xia Li, Xingjian Liu, Yao Yao, Guohua Hu, Xiaocong Xu, and Fengsong Pei. Delineating urban functional areas with building-level social media data: A dynamic time warping (dtw) distance based k-medoids method. *Landscape and Urban Planning*, 160:48–60, 2017.
- [13] Y. T. D. Cheung, M. J. Spittal, M. K. Williamson, S. J. Tung, and J. Pirkis. Application of scan statistics to detect suicide clusters in australia. *PLoS ONE*, 8:e54168, 2013.
- [14] C.-S. J. Chu, M. Stinchcombe, and H. White. Monitoring structural change. *Econometrica*, 64:1045, 1996.
- [15] S. Dasgupta and Y. Freund. Random projection trees and low dimensional manifolds. In *Proceedings of the Fortieth Annual ACM Symposium on Theory of Computing*, STOC ’08, pages 537–546, New York, NY, USA, 2008. ACM.

- [16] H. Dette and J. Gösmann. A likelihood ratio approach to sequential change point detection for a general class of parameters. *Journal of the American Statistical Association*, 115(531):1361–1377, 2020.
- [17] S. D’Heedene, K. Amaratunga, and J. Castrillón-Candás. Generalized hierarchical bases: a wavelet-ritz-galerkin framework for lagrangian fem. *Engineering Computations*, 22(1):15–37, Jan 2005.
- [18] M. Drusch, U. Del Bello, S. Carlier, O. Colin, V. Fernandez, F. Gascon, B. Hoersch, C. Isola, P. Laberinti, P. Martimort, A. Meygret, F. Spoto, O. Sy, F. Marchese, and P. Bargellini. Sentinel-2: Esa’s optical high-resolution mission for gmes operational services. *Remote Sensing of Environment*, 120:25–36, 2012. The Sentinel Missions - New Opportunities for Science.
- [19] S. Fremdt. Page’s sequential procedure for change-point detection in time series regression. *Statistics*, 48:1, 2014.
- [20] Walther G. Optimal and fast detection of spatial clusters with scan statistics. *The Annals of Statistics*, 38:1010, 2010.
- [21] M. Guerriero, P. Willett, and J. Glaz. Distributed target detection in sensor networks using scan statistics. *IEEE Transactions on Signal Processing*, 57:2629, 2009.
- [22] Jingqiu Guo, Yangzexi Liu, Qingyan Yang, Yibing Wang, and Shouen Fang. Gps-based city-wide traffic congestion forecasting using cnn-rnn and c3d hybrid model. *Transportmetrica A: Transport Science*, pages 1–22, 2020.
- [23] H. Harbrecht, M. Peters, and M. Siebenmorgen. Analysis of the domain mapping method for elliptic diffusion problems on random domains. *Numerische Mathematik*, 134(4):823–856, 2016.
- [24] Samiul Hasan, Christian M Schneider, Satish V Ukkusuri, and Marta C González. Spatiotemporal patterns of urban human mobility. *Journal of Statistical Physics*, 151(1):304–318, 2013.
- [25] D. V. Hinkley. Inference about the change-point from cumulative sum tests. *Biometrika*, 58:509, 1971.
- [26] L. Horváth, M. Hušková, P. Kokoszka, and J. Steinebach. Monitoring changes in linear models. *Journal of Statistical Planning and Inference*, 126:225, 2004.
- [27] A. Huete, K. Didan, T. Miura, E.P. Rodriguez, X. Gao, and L.G. Ferreira. Overview of the radiometric and biophysical performance of the modis vegetation indices. *Remote Sensing of Environment*, 83(1):195–213, 2002. The Moderate Resolution Imaging Spectroradiometer (MODIS): a new generation of Land Surface Monitoring.
- [28] V. Jandhyala, S. Fotopoulos, I. MacNeill, and P. Liu. Inference for single and multiple change-points in time series. *Journal of Time Series Analysis*, 34:423, 2013.
- [29] C. Kirch and S. Weber. Modified sequential change point procedures based on estimating functions. *Electronic Journal of Statistics*, 12:1579, 2018.
- [30] T. L. Lai. Sequential changepoint detection in quality control and dynamical systems. *Journal of the Royal Statistical Society, Series B*, 57:613, 1995.
- [31] Anukool Lakhina, Mark Crovella, and Christophe Diot. Diagnosing network-wide traffic anomalies. *SIGCOMM Comput. Commun. Rev.*, 34(4):219–230, aug 2004.
- [32] W.A. Light and E.W. Cheney. *Approximation theory in tensor product spaces.*, volume 1169 of *Lecture notes in mathematics*. Springer, New York, 1985.
- [33] Kulldorff M. A spatial scan statistic. *Communications in Statistics: Theory and Methods*, 26:1481, 1997.
- [34] MATLAB. *version 9.4 (R2021a)*. The MathWorks Inc., Natick, Massachusetts, 2021.
- [35] G. V. Moustakides. Optimal stopping times for detecting changes in distributions. *The Annals of Statistics*, 14:1379, 1986.
- [36] D. B. Neil and A. W. Moore. Rapid detection of significant spatial clusters. *Proceedings of the Tenth ACM SIGKDD International Conference on Knowledge Discovery and Data Mining*, page 256, 2004.

- [37] D. B. Neill. Fast subset scan for spatial pattern detection. *Journal of the Royal Statistical Society*, 74:337, 2012.
- [38] E. S. Page. Continuous inspection schemes. *Biometrika*, 41:100, 1954.
- [39] K. Pape, D. Wied, and P. Galeano. Monitoring multivariate variance changes. *Journal of Empirical Finance*, 39:54, 2016.
- [40] Anand Paul, Awais Ahmad, M Mazhar Rathore, and Sohail Jabbar. Smartbuddy: defining human behaviors using big data analytics in social internet of things. *IEEE Wireless communications*, 23(5):68–74, 2016.
- [41] Zhenghong Peng, Ru Wang, Lingbo Liu, and Hao Wu. Exploring urban spatial features of covid-19 transmission in wuhan based on social media data. *ISPRS International Journal of Geo-Information*, 9(6):402, 2020.
- [42] Natasha Petrovska and Aleksandar Stevanovic. Traffic congestion analysis visualisation tool. In *2015 IEEE 18th International Conference on Intelligent Transportation Systems*, pages 1489–1494. IEEE, 2015.
- [43] M Reed and B Simon. *Methods of modern mathematical physics 1: Functional Analysis*. Academic Press, New York, New York, 1972.
- [44] Orit Rotem-Mindali, Yaron Michael, David Helman, and Itamar M Lensky. The role of local land-use on the urban heat island effect of tel aviv as assessed from satellite remote sensing. *Applied Geography*, 56:145–153, 2015.
- [45] D.P. Roy, M.A. Wulder, T.R. Loveland, Woodcock C.E., R.G. Allen, M.C. Anderson, D. Helder, J.R. Irons, D.M. Johnson, R. Kennedy, T.A. Scambos, C.B. Schaaf, J.R. Schott, Y. Sheng, E.F. Vermote, A.S. Belward, R. Bindschadler, W.B. Cohen, F. Gao, J.D. Hipple, P. Hostert, J. Huntington, C.O. Justice, A. Kilic, V. Kovalskyy, Z.P. Lee, L. Lymburner, J.G. Masek, J. McCorkel, Y. Shuai, R. Trezza, J. Vogelmann, R.H. Wynne, and Z. Zhu. Landsat-8: Science and product vision for terrestrial global change research. *Remote Sensing of Environment*, 145:154–172, 2014.
- [46] Osvaldo E Sala, FIII Stuart Chapin, Juan J Armesto, Eric Berlow, Janine Bloomfield, Rodolfo Dirzo, Elisabeth Huber-Sanwald, Laura F Huenneke, Robert B Jackson, Ann Kinzig, et al. Global biodiversity scenarios for the year 2100. *science*, 287(5459):1770–1774, 2000.
- [47] C. Schwab and R. A. Todor. Karhunen–Loève approximation of random fields by generalized fast multipole methods. *Journal of Computational Physics*, 217(1):100 – 122, 2006. Uncertainty Quantification in Simulation Science.
- [48] X. Shao. Self-normalization for time series: A review of recent developments. *Journal of the American Statistical Association*, 110:1797, 2015.
- [49] X. Shao and X. Zhang. Testing for change points in time series. *Journal of the American Statistical Association*, 105:1228, 2010.
- [50] Shih-Lung Shaw and Daniel Sui. Introduction: Human dynamics in perspective. In *Human dynamics research in smart and connected communities*, pages 1–11. Springer, 2018.
- [51] David L Skole. Data on global land-cover change: acquisition, assessment and analysis. *Changes in land use and land cover: a global perspective*, pages 437–471, 1994.
- [52] J. Tausch and J. White. Multiscale bases for the sparse representation of boundary integral operators on complex geometry. *SIAM Journal on Scientific Computing*, 24(5):1610–1629, 2003.
- [53] D. Wied and P. Galeano. Monitoring correlation change in a sequence of random variables. *Journal of Statistical Planning and Inference*, 143:186, 2013.
- [54] Curtis E. Woodcock, Richard Allen, Martha Anderson, Alan Belward, Robert Bindschadler, Warren Cohen, Feng Gao, Samuel N. Goward, Dennis Helder, Eileen Helmer, Rama Nemani, Lazaros Oreopoulos, Joh Schott, Prasad S. Thenkabail, Eric F. Vermote, James Vogelmann, Michael A. Wulder, and Randolph Wynne. Free access to landsat imagery. *Science*, 320(5879):1011–1011, 2008.

- [55] Donald J Wuebbles, David W Fahey, and Kathy A Hibbard. Climate science special report: fourth national climate assessment, volume i. 2017.
- [56] Jason Y Zhang, Panna Felsen, Angjoo Kanazawa, and Jitendra Malik. Predicting 3d human dynamics from video. In *Proceedings of the IEEE/CVF International Conference on Computer Vision*, pages 7114–7123, 2019.
- [57] T. Zhang and L. Lavitas. Unsupervised self-normalized change-point testing for time series. *Journal of the American Statistical Association*, 113:637, 2018.
- [58] Zhe Zhu and Curtis E. Woodcock. Object-based cloud and cloud shadow detection in landsat imagery. *Remote Sensing of Environment*, 118:83–94, 2012.